The Astrophysical Journal, 883:4 (26pp), 2019 September 20 https://doi.org/10.3847/1538-4357/ab384a

Atmospheric Circulation of Brown Dwarfs and Jupiter- and Saturn-like Planets: Zonal Jets, Long-term Variability, and QBO-type Oscillations

Adam P. Showman[1,2], Xianyu Tan[2], and Xi Zhang[3]
[1] Department of Atmospheric and Oceanic Sciences, Peking University, Beijing, People's Republic of China
[2] Department of Planetary Sciences and Lunar and Planetary Laboratory, The University of Arizona, 1629 University Blvd., Tucson, AZ 85721, USA
showman@lpl.arizona.edu
[3] Department of Earth and Planetary Sciences, University of California, Santa Cruz, CA 95064, USA
Received 2018 July 22; revised 2019 July 25; accepted 2019 August 1; published 2019 September 17

Abstract

Brown dwarfs and directly imaged giant planets exhibit significant evidence for active atmospheric circulation, which induces a large-scale patchiness in the cloud structure that evolves significantly over time, as evidenced by infrared light curves and Doppler maps. These observations raise critical questions about the fundamental nature of the circulation, its time variability, and its overall relationship to the circulation on Jupiter and Saturn. Jupiter and Saturn themselves exhibit numerous robust zonal (east–west) jet streams at the cloud level; moreover, both planets exhibit long-term stratospheric oscillations involving perturbations of zonal wind and temperature that propagate downward over time on timescales of ∼4 yr (Jupiter) and ∼15 yr (Saturn). These oscillations, dubbed the quasi-quadrennial oscillation (QQO) for Jupiter and the semiannual oscillation (SAO) on Saturn, are thought to be analogous to the quasi-biennial oscillation (QBO) on Earth, which is driven by upward propagation of equatorial waves from the troposphere. To investigate these issues, we here present global, three-dimensional, high-resolution numerical simulations of the flow in the stratified atmosphere—overlying the convective interior—of brown dwarfs and Jupiter-like planets. The effect of interior convection is parameterized by inducing small-scale, randomly varying perturbations in the radiative–convective boundary at the base of the model. Radiative damping is represented using an idealized Newtonian cooling scheme. In the simulations, the convective perturbations generate atmospheric waves and turbulence that interact with the rotation to produce numerous zonal jets. Moreover, the equatorial stratosphere exhibits stacked eastward and westward jets that migrate downward over time, exactly as occurs in the terrestrial QBO, Jovian QQO, and Saturnian SAO. This is the first demonstration of a QBO-like phenomenon in 3D numerical simulations of a giant planet.

Key words: brown dwarfs – planets and satellites: atmospheres – planets and satellites: individual (Jupiter, Saturn) – turbulence – waves

1. Introduction

A variety of evidence now indicates the existence of a vigorous atmospheric circulation on brown dwarfs, which are fluid hydrogen objects thought to form like stars but with insufficient mass to fuse hydrogen, and which resemble hot, high-gravity versions of Jupiter in many ways. Infrared (IR) spectra indicate the presence of clouds and chemical disequilibrium, both of which require vertical mixing (see reviews by Helling & Casewell 2014 and Marley & Robinson 2015). IR variability occurring on rotational timescales implies that the cloud and temperature patterns are commonly patchy on regional-to-global length scales (e.g., Artigau et al. 2009; Radigan et al. 2012; Apai et al. 2013, 2017; Wilson & Rajan 2014; Buenzli et al. 2015; Metchev et al. 2015; Yang et al. 2016; Miles-Páez et al. 2017; for reviews, see Biller 2017 and Artigau 2018). The shapes of IR light curves often evolve significantly over several rotation periods, implying that the spatial patterns of clouds and temperatures change rapidly. Doppler imaging maps allow the surface patchiness to be explicitly resolved (Crossfield et al. 2014), and detailed IR spectral retrievals hold similar promise for multiwavelength light curve observations (Karalidi et al. 2016). Moreover, comparison of observations over longer epochs now holds the promise of placing constraints on the long-term evolution of the cloud structure and the underlying dynamics. The *Spitzer* Storms program (PI D. Apai), for example, has monitored six brown dwarfs at systematic intervals of up to a year (e.g., Apai et al. 2017).

These observations provide an opportunity to study how atmospheric dynamics behaves in the rapidly rotating, high internal heat flux regime applicable to brown dwarfs (see Showman & Kaspi 2013). Brown dwarfs typically receive no external stellar irradiation, and therefore lack the large-scale (e.g., equator-to-pole or day–night) contrasts in stellar heating that are responsible for driving the global circulation on hot Jupiters or solar system planets like Earth. However, the interiors of brown dwarfs convect vigorously as they lose heat to space, and this convection is expected to perturb the overlying, stably stratified atmosphere, generating atmospheric waves—and potentially, a large-scale atmospheric circulation that could consist of turbulence, vortices, storms, and zonal (east–west) jet streams. The rapid rotation periods of brown dwarfs (∼1–10 hr) implies that rotation should play a strong role in controlling the atmospheric dynamics, more akin to the situation on Jupiter than on the more slowly rotating hot Jupiters (Showman & Kaspi 2013). However, the interior heat flux from brown dwarfs of typically 10^3–10^6 W m^{-2} greatly exceeds Jupiter's interior flux of ∼7.5 W m^{-2} (Li et al. 2018b), suggesting that the convection may be far more vigorous, and the greater atmospheric temperatures of brown dwarfs relative to Jupiter imply that the radiative time constants are far shorter. As yet, the atmospheric dynamics and behavior that occur in this regime are poorly understood. Nevertheless, variability of

some Y dwarfs with effective temperature of only a few hundred Kelvins has been detected (Cushing et al. 2016; Esplin et al. 2016; Leggett et al. 2016; see also Skemer et al. 2016 and Morley et al. 2018). Atmospheric circulation of these relatively cool objects may bridge the gap between that of most observable T and L dwarfs on the one hand, and Jupiter and Saturn on the other.

Jupiter and Saturn themselves exhibit atmospheric circulations dominated by numerous zonal jet streams, including a broad, fast, eastward jet at the equator, and alternating eastward and westward jet streams in the mid-to-high latitudes; for reviews, see Ingersoll et al. (2004), Vasavada & Showman (2005), Del Genio et al. (2009), Showman et al. (2019), and Sánchez-Lavega et al. (2019). Wind speeds are typically 30 m s^{-1} on Jupiter and 100 m s^{-1} on Saturn in the mid-to-high latitudes, but reach faster speeds in the equatorial jet—approximately 100 m s^{-1} on Jupiter and 400 m s^{-1} on Saturn. The zonal jet structure is associated with latitudinal temperature variations of ~3–5 K, a zonally banded cloud pattern, and a wealth of eddies, ranging from coherent vortices like Jupiter's Great Red Spot to smaller, highly time-variable storms, vortices, and turbulence. Additionally, both planets exhibit oscillations in the stratospheric jet and temperature structure at low latitudes, in which vertically stacked eastward and westward jets—and associated temperature anomalies—slowly migrate downward over time. On Jupiter, this oscillation has a period of ~4 yr and has been dubbed the quasi-quadrennial oscillation or QQO (Leovy et al. 1991; Orton et al. 1991), whereas on Saturn it has a period of ~15 yr and is called the Saturn semiannual oscillation or SAO (Fouchet et al. 2008; Orton et al. 2008; Guerlet et al. 2011; Guerlet et al. 2018; for a review, see Showman et al. 2019).[4] These oscillations are thought to be analogous to the well-studied quasi-biennial oscillation (QBO) here on Earth, which is driven by the absorption in the stratosphere of upwardly propagating, convectively generated waves from the troposphere, and which exerts a variety of influences on global climate (Baldwin et al. 2001).

Only a few studies of the atmospheric circulation of brown dwarfs have yet been performed. Freytag et al. (2010) presented two-dimensional calculations of convection in a local box and its interaction with an overlying stably stratified layer. These models generally ignored rotation. Showman & Kaspi (2013) presented the first global models of interior convection, demonstrating the importance of rotation in the dynamics. They also constructed a theory for the characteristic wind speeds and horizontal temperature differences in the stratified atmosphere. Zhang & Showman (2014) performed global calculations of the atmospheric flow using a "one-and-a-half" layer shallow-water model, in which an active atmospheric layer overlies a deeper layer that represents the interior and was assumed to be quiescent. Convection was parameterized with a small-scale forcing, and radiation with a simple damping scheme. These simulations showed that conditions of strong forcing and/or weak radiative damping lead to a zonally banded pattern, while weak forcing and/or strong damping lead to a pattern of horizontally isotropic turbulence with no banding. Tan & Showman (2017) explored the dynamical effect of latent heating associated with condensation of silicates and iron in idealized 3D models, but did not include any representation of the (dry) convection expected to occur throughout the convection zone, which should exert significant effects on the overlying radiatively stratified atmosphere.

By comparison, numerical simulations of the global circulation on Jupiter and Saturn have a much longer history, although many aspects remain poorly explored. Such models have shown that small-scale turbulence can interact with the planetary rotation to generate zonal jets; for reviews, see Vasavada & Showman (2005), Dritschel & McIntyre (2008), Del Genio et al. (2009), and Showman et al. (2019). This line of inquiry started with two-dimensional (one-layer) models in which convection was parameterized with small-scale sources of vorticity or mass randomly injected into the layer (e.g., Williams 1978; Nozawa & Yoden 1997; Scott & Polvani 2007; Showman 2007). Thick-shell spherical convection models show how interior convection can induce the formation of zonal jets in the deep interior, although such models usually do not include a representation of the overlying atmosphere (e.g., Christensen 2002; Heimpel et al. 2005; Kaspi et al. 2009; Duarte et al. 2013). Three-dimensional models of the circulation in the stratified atmosphere have focused on jet formation by baroclinic instabilities associated with latitudinal variations in solar heating (Williams 1979, 2003; Lian & Showman 2008; Schneider & Liu 2009; Liu & Schneider 2010, 2011; Young et al. 2019) or by storm eddies associated with latent heat release (Lian & Showman 2010). Other studies impose the observed zonal-jet profile near the bottom of the domain and examine how the overlying stratospheric circulation responds to realistic radiative forcing (e.g., Friedson & Moses 2012). Note that the jet-formation processes emphasized in many of these studies—baroclinic instabilities and latent heating—are likely not relevant to brown dwarfs, where the interior (dry) convective heat flux is large, the latent heating is relatively weak, and no external irradiation gradient exists to provide externally imposed baroclinicity. The third obvious possibility—that interior dry convection directly perturbs the stably stratified atmosphere, causing the formation of zonal jets and other aspects of the atmospheric circulation (Dritschel & McIntyre 2008)—has not previously been explored in a 3D model, either for Jupiter or brown dwarfs.

To date, only a handful of studies have explored the dynamics of the Jovian QQO or Saturnian SAO (Friedson 1999; Li & Read 2000; Cosentino et al. 2017). All of these are 2D or quasi-2D models[5] that represent the latitudinal and vertical structure of the flow, but allow no longitudinal variation. Because the waves that drive these QBO-like phenomena exhibit propagation and oscillatory behavior in both longitude and height, they cannot be fully simulated in a purely 2D model, but rather must be parameterized. As yet, there exist no full 3D models of giant planets demonstrating the emergence of a QBO- or QQO-like oscillation, in which the wave generation, propagation, and absorption that can drive the oscillation are explicitly represented.

[4] Other notation has been adopted as well, particularly for the Saturnian oscillation. Guerlet et al. (2018) adopt the term Saturn Equatorial Oscillation or SEO, while Fletcher et al. (2017) adopt the more general phrase Saturnian quasi-periodic oscillation (QPO). For the Saturnian oscillation, we maintain consistency with earlier literature by using the phrase Saturnian SAO; for the general phenomenon regardless of planet or period, we adopt the phrase "QBO-like oscillation," to emphasize the links to the dynamics of the QBO—which remains much better-studied than any of the other oscillations.

[5] These investigations all solve a 2D system for the time evolution of the zonal-mean zonal wind versus latitude and height subject to parameterized wave forcing in this 2D meridional plane; 3D considerations of wave dynamics were used to determine the form this wave parameterization would take, under the assumption that the wave forcing results from a small set of specified wave modes.

Here, we present three-dimensional, global simulations of the atmospheric circulation on brown dwarfs and Jupiter- and Saturn-like planets, to explore the extent to which convection interacting with a stably stratified atmosphere can drive a circulation in the atmosphere. The simulations are idealized, in that the perturbing effects of convection near the base of the stratified atmosphere are parameterized in a highly idealized manner and the radiative heating/cooling is represented using a simple Newtonian relaxation scheme. These features provide a clean, simple environment in which the dynamical processes can be more fully diagnosed and understood. We wish to ascertain the fundamental nature of the circulation, including the existence/absence and roles of zonal (east–west) jet streams, vortices, waves, and turbulence, determine the typical wind speeds and horizontal temperature differences, and characterize the temporal variability, including that over long timescales. We show that zonal jet formation and QBO-like oscillations can occur under appropriate conditions, and we determine the sensitivity to radiative time constant and other parameters. Section 2 presents our model, Section 3 describes our results, and Section 4 concludes.

2. Model

We solve the global, spherical 3D primitive equations in pressure coordinates. These are the standard dynamical equations for a stratified atmosphere with horizontal length scales greatly exceeding the vertical length scales, as appropriate to the global-scale atmospheric flow on brown dwarfs, Jupiter, and Saturn; for reviews, see Vallis (2006) or Showman et al. (2010). To represent the effect of convection and radiation on the stratified atmosphere, we introduce source terms in the thermodynamic energy equation:

$$\frac{q}{c_p} = \frac{T_{\rm eq}(p) - T(\lambda, \phi, p, t)}{\tau_{\rm rad}} + S \quad (1)$$

where q is the specific heating rate (W kg^{-1}), c_p is the specific heat, λ is longitude, ϕ is latitude, p is pressure, and t is time.

The first term on the right-hand side of (1) represents radiative heating/cooling, which we parameterize with a Newtonian heating/cooling scheme that acts to relax the local temperature T toward a prescribed radiative equilibrium temperature, $T_{\rm eq}$, over a prescribed radiative timescale, $\tau_{\rm rad}$. On irradiated planets, day–night gradients in incident stellar flux would cause $T_{\rm eq}$ to vary spatially (e.g., being hotter on the dayside than the nightside), but for an isolated brown dwarf, the radiative-equilibrium temperature of the stratified atmosphere is determined solely by the upwelling IR radiation coming from below. Because the convection zone should exhibit minimal horizontal entropy variations, this radiative-equilibrium temperature should be nearly independent of longitude or latitude (see Showman & Kaspi 2013). Therefore, we take $T_{\rm eq}$ to be a function of pressure only. In this context, radiation acts to *remove* horizontal temperature differences—and available potential energy—and thus damps the flow.

In the observable atmosphere, radiative time constants are expected to vary greatly with temperature, and near the photosphere can be represented approximately by (Showman & Guillot 2002)

$$\tau_{\rm rad} \sim \frac{P c_p}{4 g \sigma T^3}, \quad (2)$$

where P is the photospheric pressure, g is gravity, c_p is the specific heat at constant pressure, σ is the Stefan–Boltzmann constant, and T is temperature. Inserting appropriate values for Jupiter ($P \sim 0.5$ bar, $c_p = 1.3 \times 10^4$ J kg^{-1} K^{-1}, $g = 23$ m s^{-2} and $T = 130$ K) yields $\tau_{\rm rad} \approx 6 \times 10^7$ s. This is similar to values estimated from sophisticated radiative transfer calculations providing explicit calculations of the radiative time constant as a function of pressure, which indicate that $\tau_{\rm rad}$ ranges between 10^8 and 10^7 s from 1 bar to 1 mbar (Kuroda et al. 2014; Li et al. 2018a). Nevertheless, some other studies have suggested longer radiative time constants between 10^8 and 10^9 s (Conrath et al. 1990; Guerlet et al. 2014). In contrast, at the higher temperatures of brown dwarfs, the above scaling predicts much shorter radiative time constants in the range $\sim 10^4$–10^5 s (see Showman & Kaspi 2013; Robinson & Marley 2014). To capture this range, we vary the radiative time constant from 10^4 to 10^8 s. For simplicity, we take $\tau_{\rm rad}$ constant with pressure.

Sophisticated 1D radiative-transfer models show that the temperature profile on brown dwarfs transitions from an adiabatic interior to a nearly isothermal atmosphere, with a transition at typically a few bars (e.g., Burrows et al. 2006). To mimic this behavior, we adopt a radiative-equilibrium profile

$$T_{\rm eq}(p) = (T_{\rm iso}^n + T_{\rm ad}^n)^{1/n}, \quad (3)$$

where $T_{\rm iso}$ is a constant representing the isothermal atmosphere, and $T_{\rm ad}(p)$ is an adiabatic temperature–pressure profile representing the interior, which can be expressed as $T_{\rm ad} = \theta_{\rm ad}(p/p_0)^{R/c_p}$, where $\theta_{\rm ad}$ is the potential temperature of the interior (constant for an adiabat), R is the specific gas constant, and $p_0 = 1$ bar is a reference pressure. Here, we set $T_{\rm iso} = 1000$ K and $\theta_{\rm ad} = 1500$ K, representing conditions of a typical dwarf near the L/T transition, although we emphasize that the results of our 3D simulations are insensitive to the precise values. In this notation, n is a smoothing parameter, which controls the vertical scale over which the temperature profile transitions between adiabatic and isothermal; we here take it equal to seven, which causes the transition to occur smoothly across a vertical distance comparable to a scale height. Figure 1 shows the profile $T_{\rm eq}(p)$ resulting from these choices.

The second term on the right-hand side of (1), S, represents the effect of convection on the atmosphere, specifically the perturbation of the radiative–convective boundary (RCB) by convection, as well as possible convective overshoot and mixing across the RCB. Both of these processes should occur in a highly variable manner. In principle, global convection models could provide constraints on the dominant length and timescales of this process, but such models can only be performed with unrealistic parameter settings, rendering any such predictions uncertain (Showman et al. 2011; Showman & Kaspi 2013). Instead, we choose to parameterize the forcing, giving us full control over the forcing length and timescales and allowing us to determine how they affect the atmospheric circulation. In keeping with a long history of turbulence studies, we parameterize this forcing as a random, homogeneous, isotropic source/sink in (horizontal) space, which evolves randomly in time via a Markov process (e.g., Lilly 1969; Williams 1978; Nozawa & Yoden 1997; Scott & Polvani 2007). The forcing is confined near the bottom of the domain near the RCB. Because we envision that convective plumes will push the RCB up and down, the thermal perturbations (on isobars) should remain vertically coherent

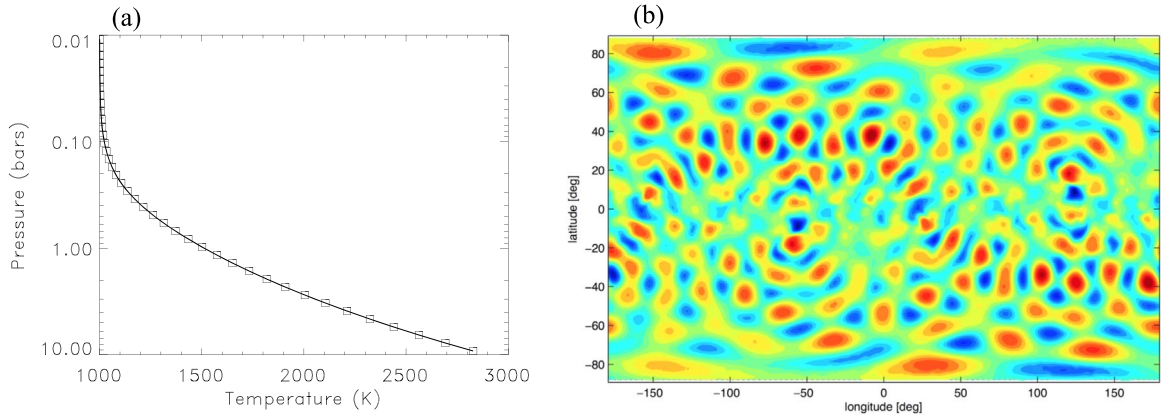

Figure 1. (Left): Radiative-equilibrium temperature–pressure profile $T_{eq}(p)$ (Equation (3)) adopted in the numerical experiments. The profile transitions from an adiabat at depth to an isotherm aloft, here with $T_{iso} = 1000$ K and $\theta_{ad} = 1500$ K. The squares show the pressures of the cell centers adopted in the 3D simulations for the example of a 40-level model. (Right): a realization of the random, horizontally isotropic forcing pattern, S_h, used in the simulation, here shown for a total forcing wavenumber $n_f = 20$.

near the RCB, and thus we adopt a forcing function of the form $S(\lambda, \phi, p, t) = S_v(p)S_h(\lambda, \phi, t)$. Here, $S_v(p)$ represents the (nondimensional) vertical structure of the forcing, which we assume to vary linearly in log-pressure from one at the base of the domain to zero one scale height above. The quantity $S_h(\lambda, \phi, t)$ represents the spatial and temporal distribution of the forcing across the globe, with units of $\mathrm{K\,s^{-1}}$. In keeping with standard procedure, this is represented as a Markovian process

$$S_h(\lambda, \phi, t + \delta t) = rS_h(\lambda, \phi, t) + \sqrt{1 - r^2}F(\lambda, \phi, t), \quad (4)$$

where r is a dimensionless memory coefficient, F represents the random modifier of S_h, and δt represents the model timestep. This formulation causes the forcing to vary smoothly from one spatially random pattern to another over a characteristic decorrelation timescale τ_{for}. The two limits of white-noise forcing and time-constant forcing would be represented as $r = 0$ and $r = 1$, respectively. For correlation timescales that are long compared to a timestep, the memory coefficient is

$$r = 1 - \frac{\delta t}{\tau_{for}}. \quad (5)$$

The forcing wavenumber n_f represents the characteristic total horizontal wavenumber on which convection perturbs the RCB. Individual convective plumes are expected to be small-scale and cannot be resolved in a global model: for example, the local, 2D box simulations of Freytag et al. (2010) suggest that individual convective plumes are typically ~10 km across—corresponding to a spherical wavenumber of 22,000 in a global model with Jupiter's radius! Despite the impossibility of resolving the individual convective plumes in a global model, it is likely that the convection will exhibit organization across a wide range of scales (as is common in Earth's tropics, for example), and in our models, the forcing wavenumber represents the supposed wavenumber of this large-scale organization. The largest possible forcing wavenumber that we can resolve numerically is $N/4$, where N is the total spherical wavenumber corresponding to the model resolution. For our nominal resolutions of C128 (see below), $N \approx 170$, implying that the largest forcing wavenumber that we can numerically resolve is $n_f = 42$. We explore values of 40 and 20. The characteristic timescale on which the large-scale convective organization varies is unknown but presumably longer than the timescale associated with individual convective plumes (associated with overshoot, for example). We perform most simulations with $\tau_{for} = 10^5$ s, but also explore 10^4 s and 10^6 s in a few integrations.

We represent the spatial structure of the forcing as a horizontally isotropic superposition of spherical harmonics of a characteristic total forcing wavenumber, n_f:

$$F = f_{amp} \sum_{m=1}^{n_f} N_{n_f}^m(\sin\phi)\cos[m(\lambda + \psi_m)], \quad (6)$$

where $N_n^m(\sin\phi)$ are the normalized associated Legendre polynomials, m is the zonal wavenumber, n is the total wavenumber, f_{amp} is the forcing amplitude in units of $\mathrm{K\,s^{-1}}$, and ψ_m is a randomly chosen phase, different for each mode. New random phases ψ_m are chosen each time (4) is evaluated, meaning that, statistically, there is no correlation in the spatial pattern of F between one timestep and the next. The Appendix presents presents simple arguments on the values of f_{amp} that are appropriate for a given heat flux and other parameters. These estimates suggest that f_{amp} of a few $\times 10^{-6}\,\mathrm{K\,s^{-1}}$ to a few $\times 10^{-5}\,\mathrm{K\,s^{-1}}$ are generally appropriate for giant planets and brown dwarfs. Although the detailed formulations differ, our overall approach of adding thermal perturbations near the bottom of the domain is similar to a scheme employed in the 3D Saturn stratospheric GCM of Friedson & Moses (2012), who introduced randomly fluctuating thermal perturbations near the tropopause as way of producing stratospheric eddies.

Because the temperature structure is nearly adiabatic at the bottom of our domain, any winds generated there would penetrate deeply into the planetary interior following the Taylor–Proudman theorem (e.g., Vasavada & Showman 2005), and at great depths, Lorentz forces may act to brake these columnar flows (e.g., Busse 2002; Liu et al. 2008; Duarte et al. 2013). We parameterize this process by introducing a frictional drag scheme near the bottom of the domain (see Schneider & Liu 2009; Liu & Showman 2013). The drag is represented in the momentum equations as $-k_v\,\boldsymbol{v}$, where $k_v(p)$ is a pressure-dependent drag coefficient and $\boldsymbol{v}$ is horizontal velocity. The drag coefficient is zero (meaning no drag) at $p \leqslant p_{drag,top}$ and varies linearly in p from zero at $p_{drag,top}$ to τ_{drag}^{-1} at the bottom of the domain, where the drag is strongest. Here, τ_{drag} represents

the timescale of this drag at the bottom of the domain. We generally adopt $p_{\rm drag,top} = 4$ bars, which is just below the RCB in our models. We consider $\tau_{\rm drag}$ to be a free parameter, which we vary over a wide range.

The domain extends from 10 bars at the bottom (below the RCB) to 0.01 bars at the top. All models adopt Jupiter's radius and a rotation period of 5 hr, which is typical for brown dwarfs (Reiners & Basri 2008), $c_p = 13{,}000\ {\rm J\,kg^{-1}\,K^{-1}}$, and $R/c_p = 2/7$, appropriate to an H_2 atmosphere. The gravity is set to either $23\ {\rm m\,s^{-2}}$ or $500\ {\rm m\,s^{-2}}$, representing objects of 1 and ~20 Jupiter masses, respectively.[6] The latter represents a typical brown dwarf, and with the former, brackets the range of gravities expected on directly imaged giant planets. The models are initialized from rest using $T_{\rm eq}(p)$ as an initial temperature–pressure profile, and are integrated until a (time-fluctuating) statistical equilibrium is reached.

Given our forcing and damping setup, our model can be considered a three-dimensional generalization of the forced-dissipative one-layer turbulence models commonly used to explore jet formation on giant planets, and in geophysical fluid dynamics (GFD) more generally (e.g., Nozawa & Yoden 1997; Scott & Polvani 2007; Sukoriansky et al. 2007; Zhang & Showman 2014).

We have kept our model formulation as simple as possible in order to provide a well-defined, clean environment in which to study jet and QBO-like dynamics. In particular, we do not include subgrid-scale parameterizations of damping due to small-scale, numerically unresolved gravity waves; rather, the jets and QBO-type oscillations here result solely from the explicitly resolved wave dynamics and their interaction with the mean flow. While small-scale gravity waves likely contribute to the momentum budgets of the actual QQO and SAO (e.g., Cosentino et al. 2017), parameterizing such waves would introduce numerous assumptions involving the directions, phase speeds, amplitudes, and spectra of the waves being parameterized, and would significantly complicate an understanding of the resulting dynamics. In our view, it is essential to first understand the behavior of resolved, idealized systems such as the one we present; only once such idealized models are understood should gravity wave parameterizations be added.

Although modest horizontal resolution is adequate for hot Jupiters (e.g., Liu & Showman 2013), brown dwarfs—like Jupiter—exhibit small Rossby deformation radii and require higher resolution. Away from the equator, the deformation radius in the stratified atmosphere is given by $L_D = NH/f$, where N is the Brunt–Vaisala frequency, H is the scale height, and $f = 2\Omega \sin\phi$ is the Coriolis parameter. Adopting a rotation period of 5 hr implies $\Omega = 3.5 \times 10^{-4}\ {\rm s^{-1}}$. For a vertically isothermal temperature profile, $NH = R\sqrt{T/c_p}$. Under brown dwarf conditions, these numbers imply $L_D \approx 1500$–3000 km depending on latitude. Ideally, the numerical grid should resolve this scale, as well as the forcing scale.

We solved the equations using the MITgcm (Adcroft et al. 2004) in cubed-sphere geometry. Motivated by the above considerations, we generally adopt C128 (i.e., 128×128 finite-volume cells on each cube face), corresponding to an approximate global resolution of 512×256 in longitude and latitude, or $0.^\circ7$ per grid point (corresponding to a resolution of 800 km for an object of Jupiter radius). We also performed several simulations at C256, corresponding to global resolutions of approximately 1024×512 in longitude and latitude ($0.^\circ35$, or ~400 km per grid point), to confirm that our qualitative results are unchanged. The vertical resolution is $N_r = 40$, 80, or 160 levels. The models are generally integrated up to 5000–10,000 Earth days (25,000 to 50,000 brown dwarf rotation periods). The timestep was 100 s in most cases (50 s in a handful of the highest-resolution models). A standard, fourth-order Shapiro filter was used to control noise at the grid scale.

3. Results

3.1. Basic Flow Regime

Our key result is that, although the forcing and damping are horizontally isotropic, the interaction of the turbulence with the planetary rotation leads to a zonally banded flow pattern and the emergence of robust zonal jets over a wide range of parameters. Figure 2 illustrates this phenomenon for a series of four high-resolution models that vary the radiative time constant from 10^4 s ((a), top row) to 10^7 s ((d), bottom row). All four models are shown at times well after the flow has reached a statistical equilibrium. Temperature and zonal wind are depicted in the left and right columns, respectively, at a pressure of 0.6 bars, close to a characteristic IR photosphere pressure for typical brown dwarfs.[7]

Although dynamical activity and zonally elongated structures occur in all of the models (Figure 2), the specific jet structure, wind speeds, and temperature differences vary significantly depending on the radiative time constant. In particular, when the radiative time constant is long (10^7 s, panel (d)), zonal jets occur at all latitudes from the equator to nearly the poles. The low-latitude jets exhibit faster speeds than the high-latitude jets, a phenomenon that occurs also on Jupiter and Saturn, but the differences are not great: wind speeds for the highest-latitude jets remain a significant fraction of those for the low-latitude jets. On the other hand, at progressively shorter radiative time constants, the strong dynamical activity is confined progressively closer to the equator, and the high latitudes lack prominent zonal jets. Specifically, when $\tau_{\rm rad} = 10^6$ s, zonal banding and significant zonal winds occur from the equator to at least 60° latitude, but they weaken poleward of that latitude. The low-latitude confinement

[6] Interestingly, however, for our particular model formulation, the entire system is independent of the value of gravity. When written in pressure coordinates, the gravity never explicitly appears in the primitive equations. The gravity indirectly enters the system via the geopotential, which appears in the horizontal pressure gradient force, $-\nabla\Phi$. The geopotential, which is a dependent variable in the pressure-coordinate version of the primitive equations, is determined by vertically integrating the hydrostatic balance equation $\partial\Phi/\partial \ln p = -RT$ with respect to pressure (where here we have assumed ideal gas). If we specify the 3D temperature structure $T(\lambda, \phi, p)$ *as a function of pressure* (not as a function of height), then the geopotential $\Phi(\lambda, \phi, p)$ is independent of gravity. In more realistic models, gravity would typically enter the system via the radiative transfer—for a given opacity, the photosphere pressure, and more generally the detailed radiative heating/cooling rates, depend on the gravity. For a given atmospheric mass, the basal pressure of an atmosphere likewise depends on gravity. Thus, we would expect gravity to affect the outcome in more realistic models that include radiative transfer. In our formulation, however, the domain depth and the forcing and damping formulations (Equation (1)) are functions of pressure, and therefore the temperature structure—and indeed the entire simulation—is independent of gravity. We verified this by comparing otherwise identical models with gravities of 23 and $500\ {\rm m\,s^{-1}}$; such models behave identically.

[7] The photosphere—namely, the pressure level where the majority of radiation escapes to space—depends greatly on wavelength, as well as on the properties of any clouds that may be present. In spectral windows like the J band, it commonly probes to several bars, whereas in absorption bands such as those of water vapor, it can be a bar or less.

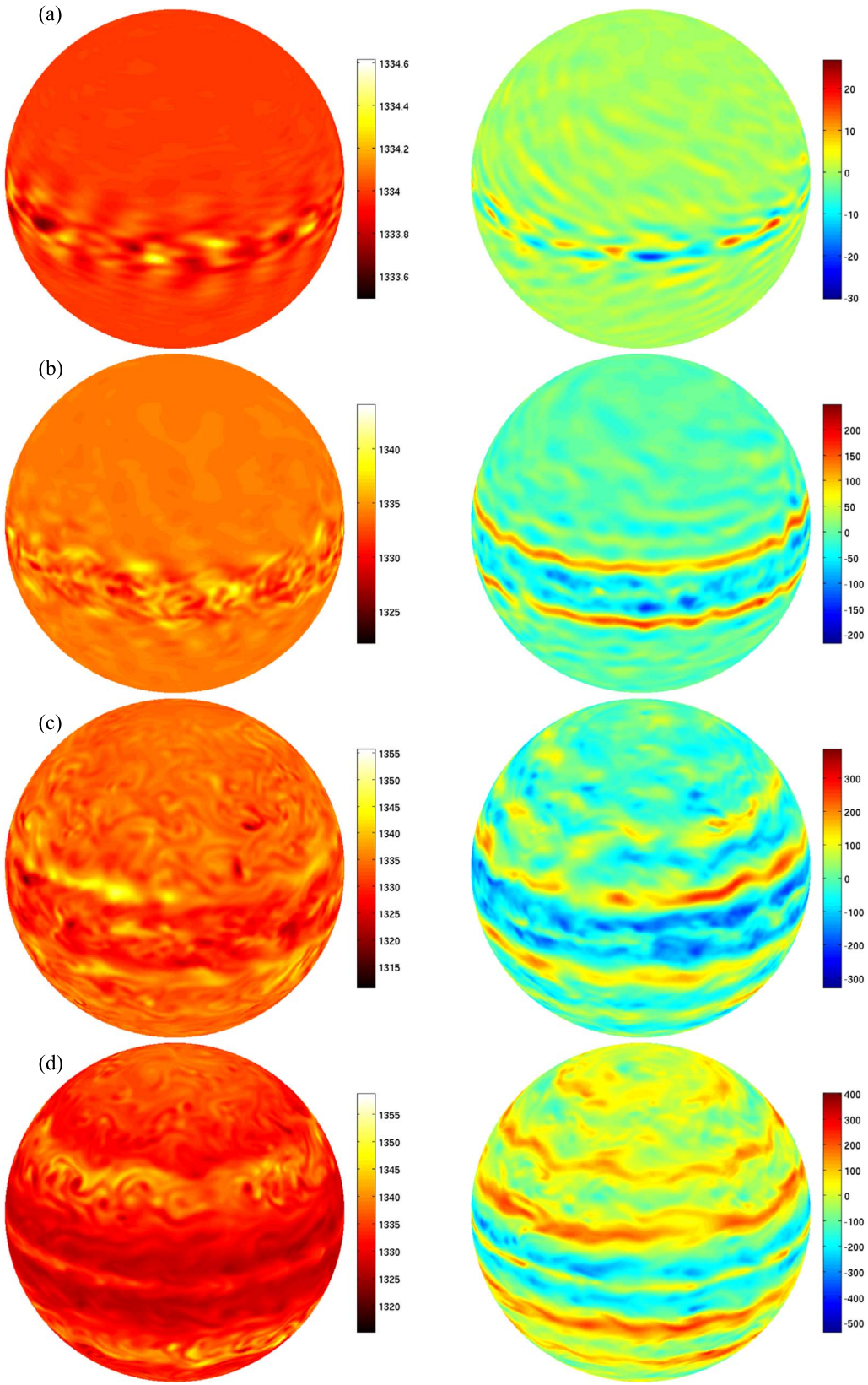

Figure 2. Temperature (K, left) and zonal winds (m s^{-1}, right) for four simulations showing the emergence of zonal jets and eddies in high-resolution 3D models of brown dwarfs. These are snapshots shown once the flow reaches a statistical equilibrium. The structure is shown at a pressure of 0.6 bars, close to a typical IR photosphere pressure for a brown dwarf. Each row shows a different simulation. The four simulations are identical except for the radiative time constant, which is 10^4, 10^5, 10^6, and 10^7 s in rows (a), (b), (c), and (d), respectively. Resolution is C128 (corresponding to a global grid of 512 × 256 in longitude and latitude) with 160 vertical levels. The forcing amplitude is $f_{\rm amp} = 5 \times 10^{-5}$ K s^{-1}, rotation period is 5 hr, gravity is 500 m s^{-2}, drag time constant is 10^6 s, convection decorrelation timescale $\tau_{\rm for} = 10^5$ s, forcing wavenumber $n_f = 20$, and other parameters are as described in the text.

becomes even more prominent at shorter radiative time constants; strong jets and horizontal temperature differences occur primarily equatorward of ∼20° latitude when $\tau_{\rm rad} = 10^5$ s and 10° latitude when $\tau_{\rm rad} = 10^4$ s. Despite this overall trend, weak dynamical activity—particularly in the wind field—nevertheless occurs at all latitudes even in the models with short radiative time constant. This can be seen in the right-hand panels of Figures 2(a) and (b). Especially at the shortest radiative time constant, this structure takes the form of weak alternating eastward and westward structures that are phase-tilted northwest–southeast in the northern hemisphere and southwest–northeast in the southern hemisphere. We identify them as barotropic Rossby waves that are generated at low latitudes by the convective forcing and propagate poleward to higher latitudes (compare to the expected phase relations in Figure 6 of Showman et al. (2013)).

The equilibrated wind speeds and horizontal temperature differences also vary systematically with the radiative time constant. As described previously, our convective parameterization represents forcing that adds energy to the model, while radiation represents damping which removes it. The statistical steady state occurs when there exists a (statistical) balance between the forcing and damping. We would thus expect the equilibrated winds and horizontal temperature differences to be greater when the convective forcing is stronger and/or the radiative damping is weaker, and the winds and temperature differences to be smaller when the convective forcing is weaker and/or the radiative damping is stronger. Our results confirm this expectation. In the models shown in Figure 2, peak-to-peak wind speeds and temperature differences are ∼1 K and ∼50–100m s^{-1} when $\tau_{\rm rad}$ is extremely short (10^4 s), but rise to ∼30 K and 900 m s^{-1} when $\tau_{\rm rad}$ is 10^7 s. Interestingly, the trend between these extremes is not smooth. The wind speeds and temperature differences increase by nearly an order of magnitude as $\tau_{\rm rad}$ increases from 10^4 to 10^5 s, but the trend weakens for further increases in $\tau_{\rm rad}$: the winds and temperature differences increase by less than a factor of two as $\tau_{\rm rad}$ rises from 10^5 to 10^6 s and then by another similar factor as $\tau_{\rm rad}$ rises from 10^6 to 10^7 s. In part, this apparent regime shift likely reflects a decrease in the importance of radiative damping relative to frictional drag as an overall energy-loss process as $\tau_{\rm rad}$ becomes large. However, there is also likely a change in the underlying dynamics because the turbulence becomes more strongly nonlinear as the flow amplitude increases.

The equatorial confinement of the zonal flow under conditions of strong damping (Figure 2) can be qualitatively understood using simple dynamical arguments (see Tan & Showman 2017). The fast rotation rates and large length scales on brown dwarfs ensure that the large-scale flow is close to geostrophic balance (Showman & Kaspi 2013). As a rule, rapid rotation and the resulting geostrophy tend to weaken the horizontal divergence relative to that expected otherwise. For a geostrophically balanced flow, the horizontal divergence is

$$\nabla \cdot \boldsymbol{v} = \frac{\beta}{f} v = \frac{v}{a \tan \phi}, \tag{7}$$

where $\boldsymbol{v}$ is the horizontal wind vector, v is the meridional (northward) velocity, a is the planetary radius, ϕ is latitude, $f = 2\Omega \sin\phi$ is the Coriolis parameter, and β is the gradient of the Coriolis parameter with northward distance, given on the sphere by $\beta = 2\Omega \cos\phi / a$. This equation approximately applies where the Rossby number, $Ro = U/fL \ll 1$, where U and L are the characteristic horizontal wind speed and length scale of the flow, respectively. For conditions relevant to our simulations ($U \sim 100$ m s^{-1} and L of a few thousand km), we expect $Ro \sim 1$ at latitudes of a few degrees; any latitude significantly poleward will exhibit $Ro \ll 1$, and thus the flow should be close to geostrophy. Equation (7) implies that, for flows close to geostrophic balance, the horizontal divergence maximizes at low latitudes and becomes zero at the poles. In addition to the divergence allowed by Equation (7), the ageostrophic component of the horizontal velocity, which is typically a fraction Ro of the geostrophic component, may be associated with significant horizontal divergence, and again this component of the horizontal divergence is likely to be greater at low latitudes due to the latitude dependence of the Coriolis parameter f. The greater horizontal divergence at low latitudes permits greater vertical motions there, allowing greater vertical entropy advection and therefore greater horizontal temperature differences than at higher latitudes (Figure 2(a) and (b)). Moreover, the greater horizontal divergence leads to efficient generation and radiation of Rossby waves at low latitudes (see discussion in Schneider & Liu (2009)), which promotes zonal jet formation and helps to explain the predominance of jets at low latitudes in our short-$\tau_{\rm rad}$ models. (The greater value of β at low latitudes than high latitudes also makes it easier to generate Rossby waves at low latitudes, but by itself this factor does not depend on $\tau_{\rm rad}$).

The zonal jet speeds and properties in our models also depend significantly on the strength of frictional drag imposed at the bottom of the model. Figure 3 shows four models with, respectively, $\tau_{\rm drag}$ of ∞ (meaning no basal drag), 10^7, 10^6, and 10^5 s, from top to bottom. All other parameters are identical, including a radiative timescale of 10^6 s and a forcing amplitude of 5×10^{-6} K s^{-1}. Note that, in all of these cases, the frictional drag is applied only at pressures greater than 4 bars near the bottom of the model; the upper atmosphere remains free of large-scale drag (though the model's Shapiro filter is applied everywhere). The zonal jets are extremely well-developed in the weak-drag models (Figure 3(a) and (b)), and well-developed but weaker in the intermediate-drag model (Figure 3(c)). In the model with strongest drag, however, a zonal jet is prominent only at the equator. These results imply that, as with radiative damping, strong frictional drag can have the effect of confining robust zonal jets to low latitudes. Poleward of this critical latitude (∼45° and ∼10°, respectively, in panels (c) and (d) of Figure 3), prominent flow structures nevertheless occur. These structure exhibit a preferential northwest–southeast tilt in the northern hemisphere and southwest–northeast tilt in the southern hemisphere, again reminiscent of Rossby-wave propagation, similar to the behavior in our models with strong radiative damping (compare Figure 3(c) and (d) to Figure 2(a)).

The wind speeds also vary significantly with drag strength; they range from over 400 m s^{-1} in the drag-free case to ∼80 m s^{-1} when drag is strongest (still, this is a modest variation considering the drag amplitude varies by orders of magnitude across this range). Interestingly, weak drag promotes strong zonality of the zonal jets, in the sense that the jets are relatively zonally symmetric and exhibit a zonal-mean zonal wind that is comparable to or significantly greater than the wind amplitude

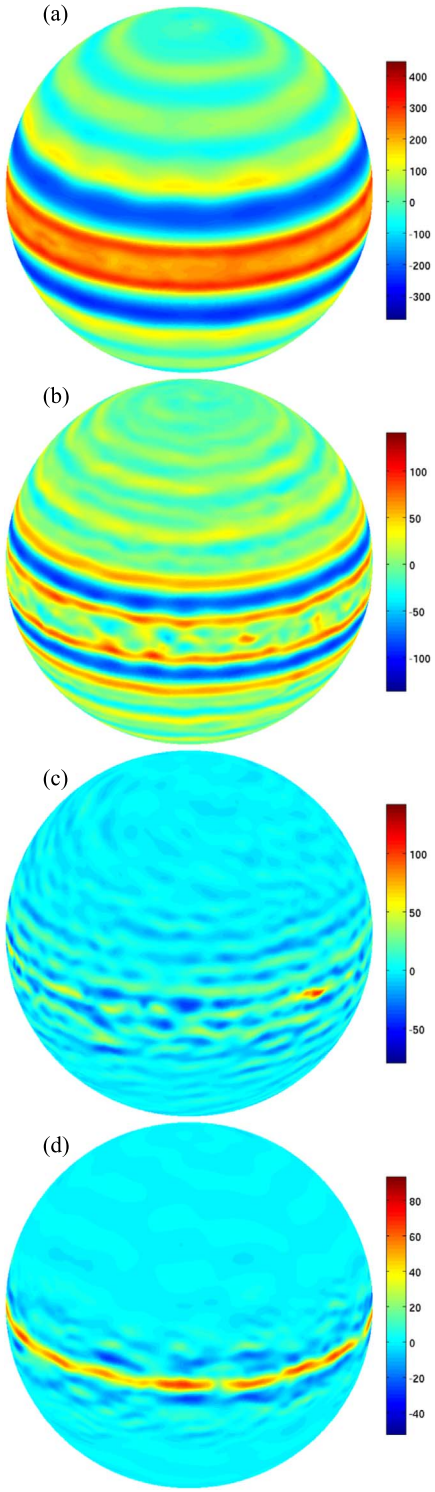

Figure 3. Zonal winds (m s^{-1}) for four simulations illustrating the dependence of the jets on bottom drag. These are snapshots taken once the flow reaches a statistical equilibrium. The structure is shown at a pressure of 0.77 bars, close to a typical IR photosphere pressure for a brown dwarf. Each row shows a different simulation. The four simulations are identical except for the frictional drag time constant, which is 10^{∞} (meaning no basal drag), 10^7, 10^6, and 10^5 s in (a), (b), (c), and (d), respectively. Resolution is C128 (corresponding to a global grid of 512 × 256 in longitude and latitude) with 160 vertical levels. The forcing amplitude is $f_{amp} = 5 \times 10^{-6}$ K s^{-1}, rotation period is 5 hr, gravity is 500 m s^{-2}, radiative time constant is 10^6 s, convection decorrelation timescale $\tau_{for} = 10^5$ s, forcing wavenumber $n_f = 20$, and other parameters are as described in the text.

of the small-scale eddies that coexist with the jets. For example, the weak-drag model in Figure 3(a) exhibits similar wind speeds to the model from Figure 2(c) that features both stronger force and stronger drag, but the zonal jets are much more regular and zonally symmetric in the former model than the latter. This result is readily understood from the fact that the feedbacks that reorganize the turbulence into a banded structure take time to operate; when forcing and damping are weak, the timescales on which they modify the flow properties are long and the dynamical reorganization of the turbulence into a banded pattern can occur relatively unimpeded. In contrast, strong forcing and damping tend to modify the flow properties on short timescales, partially disrupting the dynamical "zonalization" process as it occurs.

The jet speeds and properties also depend significantly on the forcing amplitude. An example can be seen by comparing Figures 2(c) and 3(c). The former adopts a forcing amplitude ten times greater than the latter (5×10^{-5} versus 5×10^{-6} K s^{-1}); all other parameters are identical between the simulations, including radiative and drag timescales that are both 10^6 s. At greater forcing, the typical jet speeds reach ±100 m s^{-1}, with peak speeds exceeding 300 m s^{-1}. With a forcing ten times weaker, the characteristic speeds are just tens of m s^{-1}, and exceed 50 m s^{-1} in just a few locations. The prominent low-latitude jets that exist equatorward of ∼45° latitude are also significantly narrower, more closely spaced in latitude, and appear to exhibit greater zonal symmetry in the weaker-forcing model.

3.2. Vorticity and Implications for Mechanisms of Jet Pumping

We next turn to examine the vorticity, which provides additional information on jet formation. Figure 4 shows the absolute and relative vorticity for two different models illustrating the development of banded structure under different conditions. Absolute vorticity is defined as $\zeta + f$, where $\zeta = \boldsymbol{k} \cdot \nabla \times \boldsymbol{v}$ is the relative vorticity, and $\boldsymbol{k}$ is the local upward unit vector on the sphere. Under certain conditions, the absolute vorticity provides an approximation to the potential vorticity (PV), which is a materially conserved quantity under frictionless, adiabatic conditions (Vallis 2006). In a stratified atmosphere, the PV is defined as the absolute vorticity, $\zeta + f$, divided by a measure of the vertical spacing between isentropes, which can vary spatially and temporally due to atmospheric dynamics. However, in highly stratified regions with modest horizontal temperature perturbations, the primary contribution to PV variations are due to the variations in absolute vorticity rather than thermal structure.

In situations when robust zonal jets emerge, our models tend toward a state where the absolute vorticity, $\zeta + f$, becomes nearly homogenized within zonal strips, with relatively sharp meridional gradients in absolute vorticity at the edges of adjacent strips. This is clearly illustrated in Figure 4 (leftmost panels); the top row represents a weakly forced, weak-friction model whose resulting jets are nearly zonally symmetric with relatively modest eddy activity; the bottom row represents a more strongly forced, strong-friction model with stronger eddies (these are just the two models from Figures 3(a) and 2(d), respectively). In both cases in Figure 4, the homogenization of absolute vorticity in zonal strips manifests clearly as discrete bands of differing colors, ranging from blue in the southern hemisphere (where absolute vorticity is negative), to red in the northern hemisphere (where it is positive). At the

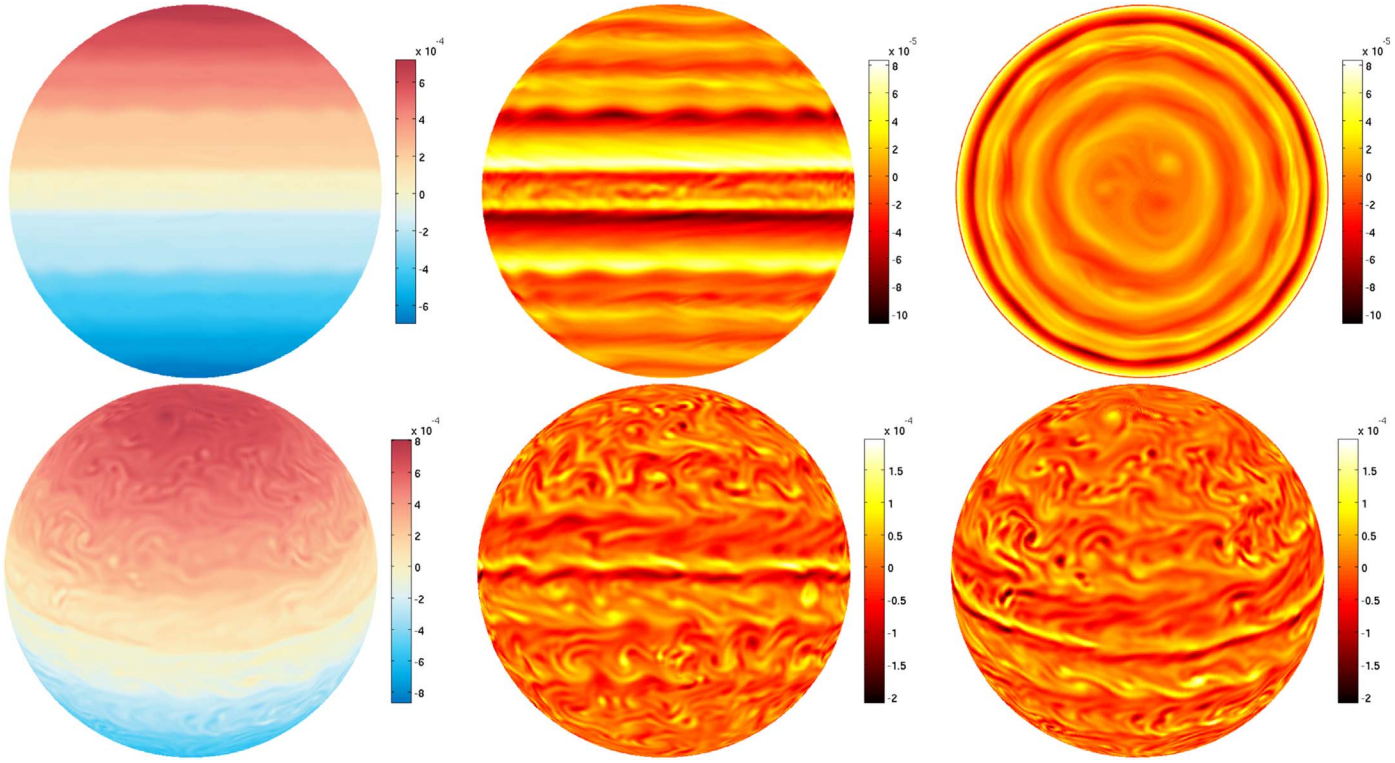

Figure 4. Vorticity structure illustrating the development of banding in two models—a weakly forced, weakly damped model in the top row, and a more strongly forced, strongly damped model in the bottom row. The left panels shows the absolute vorticity $\zeta + f$ (with equatorward and oblique viewing angles in the top and bottom rows, respectively). The middle and right-hand panels show the relative vorticity ζ. The middle column shows the view from the equatorial plane. On the right, the top panel shows the view looking down over the north pole, and the bottom panel shows an oblique view. Note the organization into strips of nearly constant absolute vorticity, as well as the existence of turbulent filamentary structures and edge waves between the strips. The top row is the same model as in Figure 3(a), with $\tau_{\rm rad} = 10^6$ s, $\tau_{\rm drag} = \infty$, and $f_{\rm amp} = 5 \times 10^{-6}$ K s^{-1}. The bottom row is the same model as in Figure 2(d), with $\tau_{\rm rad} = 10^7$ s, $\tau_{\rm drag} = 10^6$ s, and $f_{\rm amp} = 5 \times 10^{-5}$ K s^{-1}.

boundaries between the strips, the absolute vorticity gradients are relatively sharp. The strips are more prominent in the weakly forced, weak-friction model than in the strongly forced, strong-friction model, a result also seen in highly idealized one-layer turbulence studies (e.g., Scott & Dritschel 2012). The relationship between vorticity and winds implies that the boundaries between strips correspond to the latitudes of the eastward zonal jets, whereas the interior of the strips themselves (where PV approaches a homogenized state) correspond to to the latitudes of westward jets (see, e.g., the discussion in Dritschel & McIntyre (2008)). The zonal-mean zonal winds, absolute vorticity, and relative vorticity for the former model are illustrated in Figure 5, where the absolute vorticity staircase is evident, and the correspondence between the latitudes of the jets and the staircase steps can be seen. The tendency to develop PV staircases, analogous to those in our models, has also been observed on Jupiter and Saturn (e.g., Read et al. 2009).

In some models, a robust eastward equatorial jet—atmospheric superrotation—develops. If this eastward jet were sharp (with a single, sharp local maximum of zonal wind at its core, centered at the equator) then this would be associated with a sharp jump (discontinuity) in absolute vorticity centered on the equator. In cases such as Figure 5, however, the superrotation exhibits "cusps," wherein the zonal wind within the superrotating jet maximizes on either side of the equator, with a shallow local minimum of zonal wind right on the equator. In this case, the region between the cusps corresponds to a zonal strip of (partially) homogenized absolute vorticity, centered on the equator, as seen in Figures 4 and 5(b). This strip tends to be narrower in latitudinal extent than the zonal strips of homogenized absolute vorticity at higher latitudes.

The boundaries between strips meander more substantially in longitude in the more strongly forced model, and numerous turbulent, filamentary structures can be seen in that case (Figure 4, bottom row). These represent the role of PV mixing due to breaking Rossby waves, which in some cases can breach the PV barriers and cause mixing between the strips, leading to filamentary structures with local minima or maxima of PV within any given strip. The relative vorticity structure (Figure 4, middle and right-hand panels) likewise shows a prominent banded structure with superposed eddies. Both models show quite strikingly the existence of oscillatory wave structures at the boundaries between the zonal strips of nearly constant absolute vorticity; these meanders can be thought of as "edge" Rossby waves whose restoring force results in large part from the quasi-discontinuous jump in PV from one strip to the next.

The organization of the flow into strips of nearly constant absolute vorticity suggests that Rossby wave breaking plays a critical role in zonal jet formation in these models. Rossby wave breaking tends to occur preferentially in regions of weaker meridional PV gradient, and the wave breaking causes mixing that tends to decrease the (zonal-mean) meridional PV gradient still further. This leads to a positive feedback: given modest initial variations of meridional PV gradient as a function of latitude,

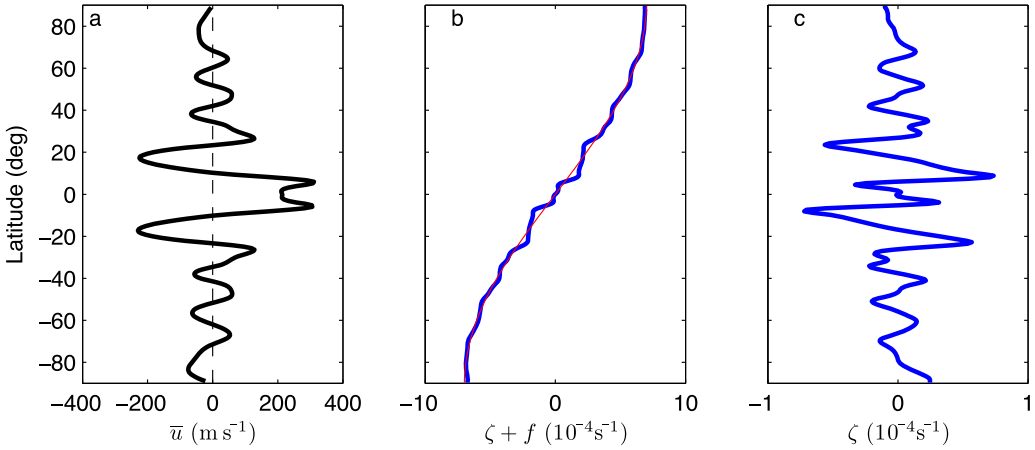

Figure 5. Zonal-mean zonal wind, absolute vorticity, and relative vorticity at 1.5 bars for a model exhibiting a flow field qualitatively similar to Jupiter and Saturn, with strong equatorial superrotation and numerous higher-latitude eastward and westward jets. Note that, in this case, the equatorial superrotation is a steady feature. The absolute vorticity becomes nearly homogenized in strips, the edges of which occur at the latitudes of the eastward jets. Relative vorticity exhibits the characteristic sawtooth pattern one expects for a flow exhibiting such absolute-vorticity homogenization. This is the same model as in the top rows of Figures 3 and 4.

Rossby-wave breaking will preferentially occur at the latitudes of weaker PV gradient, and the lessening of the PV gradient due to the wave breaking in those regions allows wave breaking to occur even more easily at those latitudes, lessening the PV gradient still further. The end state is a flow where PV is almost totally homogenized in strips, with sharp PV discontinuities in between; for reviews of the mechanism, see Dritschel & McIntyre (2008) and Showman et al. (2013). Research using idealized, high-resolution one-layer models shows that this idealized limit is achieved most readily under conditions of weak forcing and damping; in contrast, stronger forcing and damping can cause PV sources/sinks, as well as mixing between the strips, that partially smooths the staircase pattern and prevents complete PV homogenization within the strips (e.g., Scott & Dritschel 2012). This helps explain why the staircase pattern is more prominent in the weakly forced/damped simulation than the strongly forced/damped simulation in Figure 4. As an initial flow slowly self-organizes into a banded state due to this mechanism, the defining relationship between PV and winds will imply the existence of eddy momentum fluxes that transport eastward momentum out of westward jets into the cores of eastward jets—helping to generate the jets and (once they are equilibrated) maintain them against frictional and radiative damping.

3.3. Low-latitude QBO-like Oscillations

Our simulations commonly show the emergence of a long-term, multi-annual oscillation in the low-latitude zonal-jet and temperature structure, analogous to the terrestrial QBO, the Jovian QQO, and the Saturnian SAO. Figure 6 shows examples of this oscillation for two simulations, one (top row) with stronger basal drag ($\tau_{\rm drag} = 10^6$ s) and the other (bottom row) with weaker basal drag ($\tau_{\rm drag} = 10^7$ s); both simulations adopt a radiative time constant of 10^6 s. The figure shows the zonal wind over the globe on a constant-pressure surface of 0.2 bars at three snapshots at different times, increasing from left to right within each row. The times of these snapshots are not at regular intervals, but rather are chosen to illustrate the extrema of the oscillation over one cycle. At the beginning of the depicted oscillation cycle, the equatorial jet is eastward, with a speed of about 100 m s^{-1} (left panels, Figures 6(a) and (d)). At intermediate times, thousands of days later, the equatorial jet has reversed direction entirely at 0.2 bars, and now flows westward, with a zonal wind speed of about -100 m s^{-1} (middle panels, Figures 6(b) and (e)). At even later times, however, the equatorial jet has flipped back to its eastward configuration (right panels, Figures 6(c) and (f)), and the overall structure resembles that in Figures 6(a) and (d). The total oscillation period is approximately 4400 and ~7000 days (12 and 19 yr) in these two models, respectively.

In models where this oscillation occurs, the low-latitude regions generally contain *both* an eastward zonal jet *and* a westward zonal jet at any given time—in a vertically stacked configuration, with one jet overlying the other—and the entire structure migrates downward over time. This is illustrated for a particular case in Figure 7, which shows the vertical and latitudinal structure of the zonal-mean zonal wind as a function of latitude and pressure. In the simulation shown in Figure 7, at ~6875 Earth days, there exists an eastward equatorial jet at $p \lesssim 0.03$ bars, a westward equatorial jet from 0.05 to 0.5 bars, and an eastward equatorial jet deeper than 0.5 bars. Over time, the eastward jet near the top of the domain deepens vertically, the underlying westward jet shrinks in vertical extent, and the transition between them slowly shifts downward. Eventually, at ~8000 days, a new westward equatorial jet emerges at the top of the domain, deepening gradually in vertical extent. All of this means that, at some times during the oscillation, the structure at $p \lesssim 1$ bar comprises an eastward jet on top of a westward jet, but at other times it comprises a westward jet on top of an eastward jet. At some times, there are three or even four stacked jets of alternating sign. Figure 7 makes clear that, as these jets migrate downward, any given isobar successively experiences either eastward or westward flow, alternating in time—as seen previously in Figure 6.

The oscillation affects not only wind but also the thermal structure. Perturbations of the temperature are correlated with the wind structure and also migrate downward over time with the same period. This is shown in Figure 8, which depicts the temperature anomalies (defined here as deviations of the local, zonal-mean temperature from the reference temperature profile, $T_{\rm eq}(p)$) versus latitude and pressure for the same simulation as in Figure 7. It can be seen that the typical temperature perturbations reach about ~10 K, and that they migrate downward over time. Figure 8 shows that the temperature extrema at

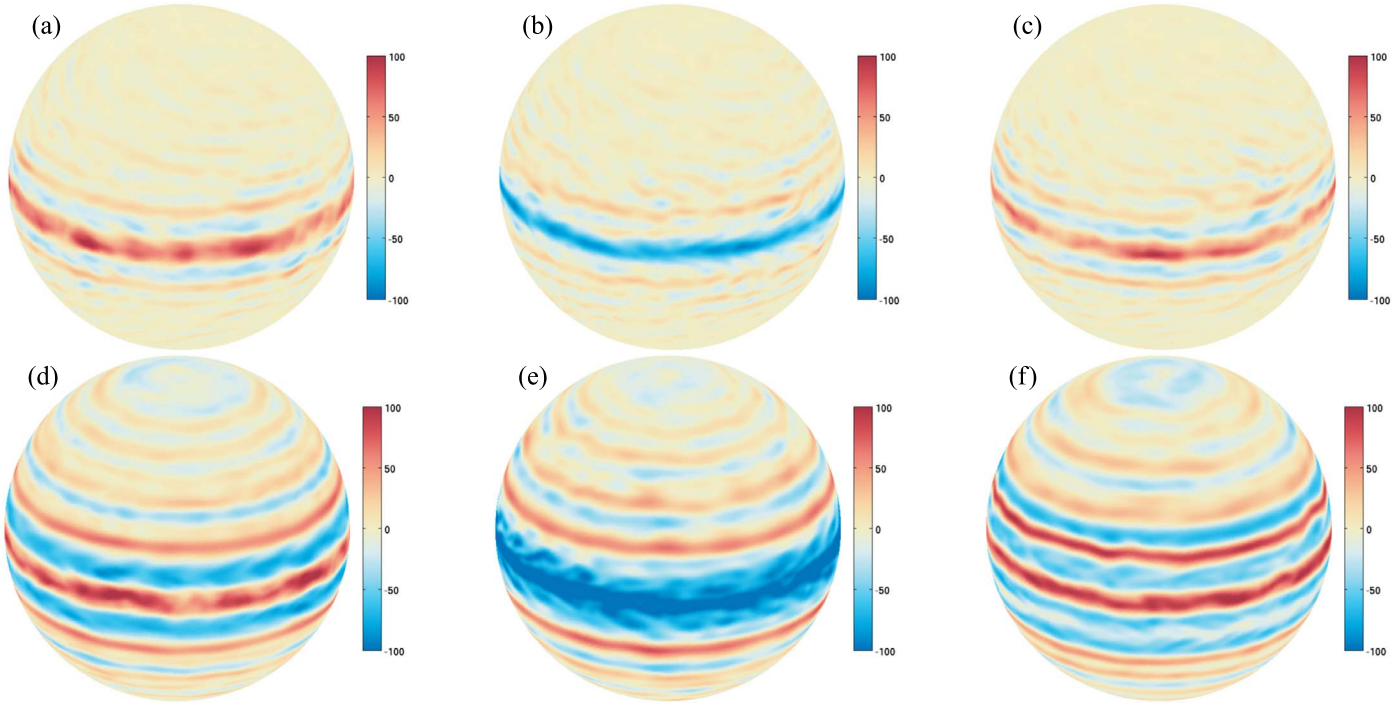

Figure 6. Zonal winds (m s^{-1}) over time in two models, illustrating a long-period oscillation in the low-latitude wind structure. Each row represents one integration with time increasing from left to right. The top row depicts a simulation with weaker jets, due to stronger drag, $\tau_{\rm drag} = 10^6$ s. The snapshots are depicted at 1389, 3588, and 5787 Earth days in (a), (b), and (c), respectively (corresponding to 6666, 17,222, and 27,778 rotation periods). The bottom row represents a simulation with stronger jets due to weaker drag, $\tau_{\rm drag} = 10^7$ s, shown at 2200, 6600, and 11,000 Earth days in (d), (e), and (f), respectively (corresponding to ∼10,500, 32,000, and 53,000 rotation periods). Note how the equatorial jet shifts from an eastward jet (equatorial superrotation), to a westward jet, and back again. The structure is shown at a pressure of 0.2 bars, close to a typical IR photosphere pressure for a brown dwarf. Resolution is C128 (corresponding to a global grid of 512 × 256 in longitude and latitude) with 160 vertical levels. In both models, the forcing amplitude is $f_{\rm amp} = 5 \times 10^{-6}$ K s^{-1}, rotation period is 5 hr, gravity is 500 m s^{-2}, radiative time constant is 10^6 s, forcing wavenumber $n_f = 20$, convective decorrelation timescale is $\tau_{\rm for} = 10^5$ s, and other parameters are as described in the text.

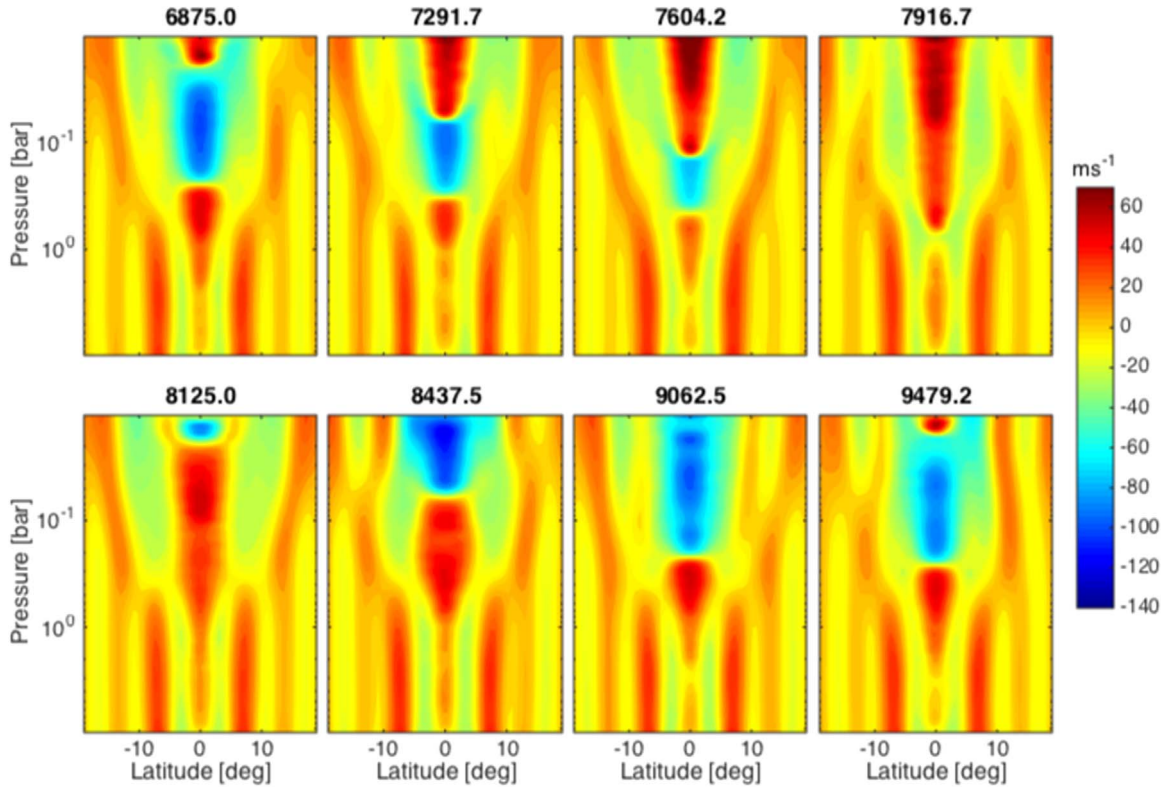

Figure 7. Time evolution of zonal-mean zonal wind (m s^{-1}) vs. latitude and pressure, showing the occurrence of a multiannual variation of the structure of the low-latitude zonal jets. Each panel depicts the structure at a specific time, shown in Earth days above the panel. This is the same model as shown in the top row of Figure 6.

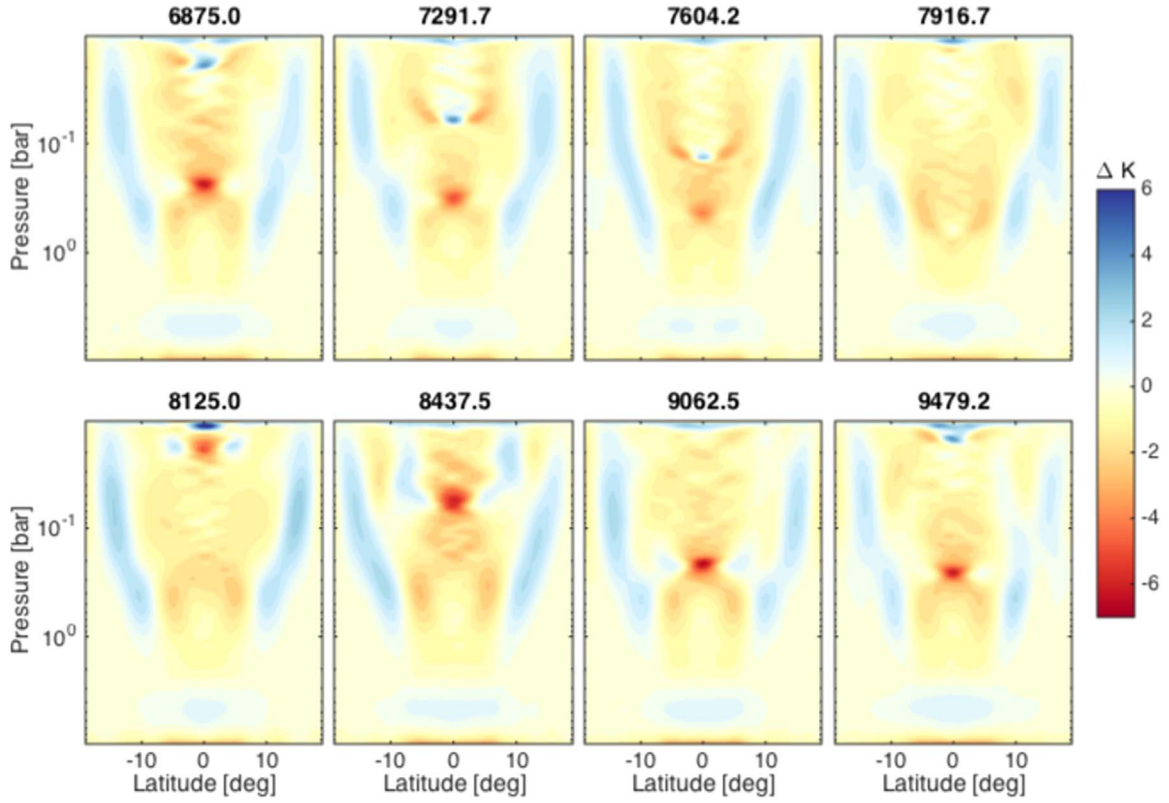

Figure 8. Time evolution of zonal-mean temperature anomaly (K) vs. latitude and pressure, showing the occurrence of a multiannual variation of the structure. Each panel depicts the structure at a specific time, listed above each panel in days. This is the same model shown in the top row of Figure 6.

the equator tend to be anticorrelated to those occurring off the equator, such that (for example) locally warm regions at the equator are flanked by locally cooler regions immediately north and south. At the fast rotation rates of brown dwarfs, the background thermal structure is close to geostrophic balance, which implies that the thermal-wind equation approximately holds (e.g., Holton & Hakim 2013, p. 82):

$$\frac{\partial u}{\partial \log p} = \frac{R}{f}\left(\frac{\partial T}{\partial y}\right)_p, \tag{8}$$

where u is zonal wind, y is northward distance on the sphere, R is the specific gas constant, and the horizontal derivative is taken at constant pressure. This equation only holds where the Rossby number is small, implying poleward of several degrees on a brown dwarf. However, if u and T in Equation (8) are taken as their zonal means, then the equation holds considerably closer to the equator, and can thus provide guidance. Equation (8) implies that regions with significant vertical shear of the zonal wind should likewise exhibit significant latitudinal temperature gradients, and this is in fact what we see in Figures 7 and 8.

Figure 9 provides another view of the vertical structure, showing how the zonal-mean zonal wind, as a function of height, evolves over time. The structure of the vertically stacked eastward and westward jets, as well as their downward evolution over time, is striking. The period is about ∼4400 days in this model. Despite the periodicity, the behavior at any given pressure is not sinusoidal throughout the cycle but exhibits a more complex structure. In particular, at low

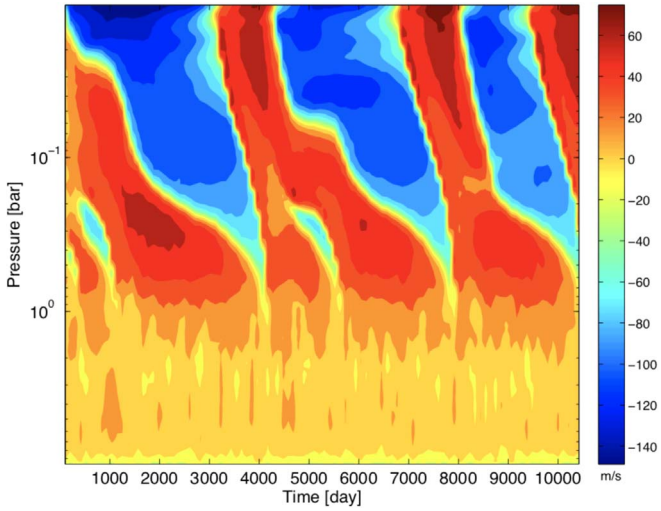

Figure 9. Zonal-mean zonal wind at the equator vs. pressure and time (in Earth days) from a model with high horizontal resolution (C128) and 160 vertical levels.

pressures, a significant fraction of the cycle is occupied by the westward phase, with the eastward phase representing significantly less than 50% of the oscillation period—but the reverse is true at greater pressures (with a transition around ∼0.2 bars). However, the detailed nature of the structure is sensitive to parameter values and differs between models.

As foreshadowed earlier, the phenomenon depicted in Figures 6–9 is extremely similar to the well-known oscillation in the Earth's stratosphere called the QBO. The QBO likewise

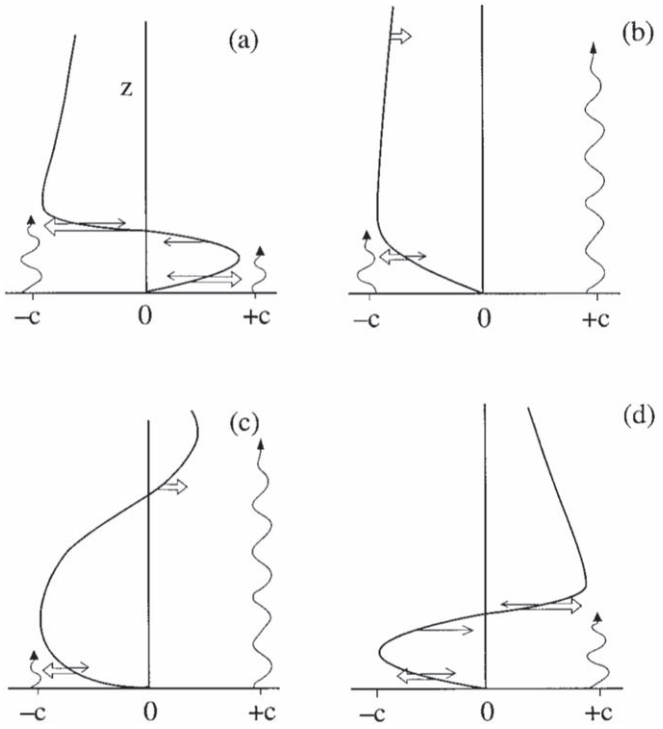

Figure 10. Schematic of the QBO mechanism. This depicts half of a cycle, from the idealized model by Plumb (1977). The curvy solid line represents the background zonal-mean zonal flow. Plumb (1977) imagined eastward and westward propagating waves, respectively depicted by $+c$ and $-c$. Preferential absorption of these waves leads to zonal accelerations that are shown by the thick double arrows. The peaks in these accelerations occur below the peaks in the jets themselves, causing the jet structure to migrate down over time. From Baldwin et al. (2001), after Plumb (1984).

involves vertically stacked eastward and westward stratospheric, equatorial zonal jets—and associated temperature anomalies—that migrate downward with a period of approximately 28 months; for reviews, see Baldwin et al. (2001) or pp. 313–331 of Andrews et al. (1987). A similar oscillation detected on Jupiter with a period of ∼4 yr is called the Quasi Quadrennial Oscillation or QQO (Leovy et al. 1991; Friedson 1999; Simon-Miller et al. 2006), and another on Saturn with a period of ∼15 yr is called the Saturn SAO (Fouchet et al. 2008; Orton et al. 2008; Guerlet et al. 2011; Guerlet et al. 2018; for a review, see Showman et al. 2019). A wide range of theoretical and modeling studies have been conducted to identify the dynamical mechanisms of the QBO, and similar dynamics are believed to control the behavior of the Jovian QQO and Saturnian SAO.

It is now widely accepted that these QBO-type oscillations result from a wave–mean-flow interaction involving the upward propagation of equatorial waves generated in the lower atmosphere and their damping and absorption in the middle and upper atmosphere (Lindzen & Holton 1968; Holton & Lindzen 1972). The fundamental mechanism is illustrated in Figure 10, based on a simple model of the phenomenon from Plumb (1977). Imagine the presence of upwardly propagating waves with both eastward and westward phase speeds. These waves are associated with a vertical flux of zonal momentum. In the absence of damping, such waves would propagate upward without causing any significant alteration to the background flow. If they are damped or absorbed, however, the resulting decrease in wave amplitude causes a divergence in the upward zonal-momentum flux, implying that the waves induce a zonal acceleration of the background flow. This allows for the emergence of zonal flows in response.

Crucially, the presence of a background zonal flow spatially organizes the wave absorption, allowing the emergence of a coherent zonal-jet structure that evolves in time. Generally, absorption of an eastward- or westward-propagating wave causes a corresponding eastward or westward acceleration of the background flow. Simultaneous damping of both eastward- and westward-propagating waves in a single location leads to counteracting accelerations that partly cancel out. However, in the presence of zonal flow, eastward- and westward-propagating waves damp at differing rates, causing a preferential net acceleration that is either eastward or westward. For example, in the presence of a weak eastward zonal flow, eastward-propagating waves exhibit reduced vertical group velocity, allowing them to be more easily damped than westward propagating waves—thereby promoting a net eastward acceleration. Plumb (1977) showed that, because of this mechanism, a state with initially zero zonal-mean zonal flow is unstable and will, over time, develop vertically stacked eastward and westward jets. Once these jets are sufficiently strong, upward-propagating waves can encounter critical levels on the lower flanks of these jets: layers where the background zonal jet speed equals the zonal phase speed of the upward-propagating wave. Waves that encounter critical levels tend to be absorbed at an altitude close to the critical level, causing a zonal acceleration of the same sign as the background wind. Because such critical levels are located on the bottom flank of the jet, the peak zonal acceleration will occur *below* the maximum of eastward zonal wind, and this causes the jet to migrate downward over time. As shown in Figure 10(a), an eastward jet will absorb eastward-propagating waves but tends to be transparent to westward-propagating waves, which propagate through the eastward jet until they reach an overlying westward jet, where they can be preferentially damped or absorbed. In this way, vertically stacked jets of both eastward and westward phases propagate downward over time (Figure 10(b)–(d)).

In Earth's atmosphere, the waves responsible for driving the QBO result primarily from tropospheric convection and exhibit a range of length scales and periods. The dominant wave types include large-scale modes such as the eastward-propagating Kelvin wave and westward-propagating mixed Rossby-gravity (MRG) and Rossby waves, as well as smaller-scale inertia-gravity and gravity waves of both eastward and westward phases (e.g., Baldwin et al. 2001). The equatorial confinement of the main jet structure within the QBO arises from the fact that many of the waves responsible for driving it are equatorially trapped, as well as because, in the extratropics, wave-induced accelerations are cancelled out, to large degree, by Coriolis accelerations due to a mean-meridional circulation triggered by the wave forcing, whereas in the tropics, where the Coriolis force is weaker, a greater fraction of the wave torques are able to cause a net acceleration of the zonal wind (Baldwin et al. 2001). In our models, the convective forcing has sufficiently low wavenumber ($\lesssim$40) that it will primarily trigger the large-scale class of wave modes, and we have intentionally excluded any subgrid-scale parameterizations of small-scale, numerically unresolved gravity waves. The resolved waves that drive the QBO-like oscillations in our models are therefore large-scale waves such as the Kelvin waves, Rossby waves, and MRG waves. We provide a detailed

analysis of the wave modes and how they influence the mean flow in Section 3.4.

In most of our simulations exhibiting QBO-type phenomena, the oscillation period is between ∼1000 and 10,000 Earth days, depending on parameters. One expects that the characteristic timescale, wavenumber, and amplitude of the convective forcing will control the population of upwardly propagating waves, which will strongly shape the oscillation period of the QBO-type phenomenon (e.g., stronger convective forcing amplitude could lead to stronger wave amplitudes and shorter QBO oscillation periods). Similarly, radiative and frictional damping can affect both the jet structure—modifying the speed and meridional structure of the jets—and the convectively generated waves themselves, and thus should likewise influence the QBO oscillation period, as well as whether the oscillation occurs at all. Although we have run a variety of simulations exhibiting QBO-type oscillations, the computational expense of these high-resolution models makes it difficult to systematically characterize how all these parameters quantitatively influence the QBO properties, a task we leave to the future.

We also note the importance of vertical resolution, as the convectively generated waves that drive the QBO have short vertical wavelengths near their critical levels, which requires high vertical resolution to capture adequately. Terrestrial GCMs with coarse vertical resolution generally fail to generate a QBO, and only once vertical resolution exceeds 40–50 levels does a realistic QBO-like oscillation emerge, albeit not necessarily with the detailed properties of the actual terrestrial QBO (e.g., Takahashi 1996, 1999). Interestingly, in the parameter regimes where the QBO-type oscillation can occur, our models with 40, 80, and 160 vertical levels all exhibit such QBO-type oscillations, but the period and other details of the oscillation differ between these models. For example, in one set of otherwise identical models, we found that the oscillation period changed from 4.1 to 5.7 to 7.1 yr as the resolution was increased from 40 to 80 to 160 vertical levels. The sensitivity of the oscillation amplitude appears to be much more modest, however; the eastward and westward phases of the oscillation in these models have peak zonal wind speeds of ∼70 and $-120\ \mathrm{m\ s^{-1}}$, essentially independent of resolution, across this entire set. The vertical-resolution sensitivity of the oscillation period may result in part from overly coarse resolution of the critical-level wave-absorption regions, but also from overly coarse resolution of the parameterization of convective perturbations to the RCB at the bottom of the model, when too few levels are used. The basal forcing region is only a few levels thick in the lowest-resolution models; it is possible that changes to the vertical resolution are influencing the effective model forcing amplitude, which in turn would influence the resulting wave amplitudes and momentum fluxes driving the QBO-like oscillation. Regardless of the details, these results demonstrate that vertical resolutions of 40 and 80 levels are insufficient, and even for 160 levels we cannot as yet guarantee full numerical convergence. (In contrast, the properties of the off-equatorial jets—poleward of ∼10° latitude—appear to be largely similar over the full range of vertical resolutions we explored, from 40 to 160 levels.) Future detailed work will be necessary to explore the resolution sensitivity at extreme vertical resolutions.

The QBO-like oscillations captured here are an example of an emergent property that results from the nonlinearity of the system. In the simulations in Figures 6–9, all the explicit timescales in the system (namely the radiative, drag, and convective forcing timescales) are short, on the order of tens of days or less—yet the oscillation that emerges has timescales of thousands of days. This is a fascinating example of long-term "memory" that the system exhibits due to its internal dynamics, even when all explicit forcing and damping timescales are shorter by orders of magnitude. This emergent behavior differs strongly from the behavior exhibited by a linear system, where one expects the response and the forcing to have identical frequencies.

As a result, it is natural to expect that—even though brown dwarfs have short radiative time constants of $\sim 10^6$ s or less, and presumably short convective timescales as well—the atmospheric circulations on brown dwarfs could nevertheless exhibit ultra-long-time variability that would manifest in long-term monitoring surveys. This provides motivation for continuing to monitor specific brown dwarfs over periods of years, to search for multiannual variability, as they may well have variability on such long timescales in addition to the shorter-term variability that is typically the emphasis of current surveys.

3.4. Waves and Role in Driving the QBO-like Oscillation

Here, we demonstrate the role of waves in driving the QBO-like oscillations, characterize the wave population, and investigate the wave modes specifically responsible for driving the oscillations in our models. For concreteness, we focus on one particular model experiment, namely the one shown in the top row of Figure 6, which is also the same one depicted in Figures 7–9.

We first determine the forcing of the zonal-mean zonal flow caused by waves, and show that it has the structure necessary to drive a QBO-like oscillation. The role of waves and eddies in driving the mean flow can be quantified using the framework of the "Transformed Eulerian Mean" (TEM) equations, which provide a representation for the evolution of the zonal-mean zonal wind and meridional circulation in response to waves, radiation, and other effects (e.g., Andrews et al. 1983, 1987). The TEM zonal-momentum equation in pressure coordinates is

$$\frac{\partial \overline{u}}{\partial t} = \left[-\left(\frac{1}{a\cos\phi} \frac{\partial (\overline{u}\cos\phi)}{\partial \phi} - f \right) \overline{v}^* - \frac{\partial \overline{u}}{\partial p} \overline{\omega}^* \right] + \frac{1}{a\cos\phi} \nabla \cdot \boldsymbol{F} + \overline{X}. \quad (9)$$

Here, all variables have been decomposed into their zonal means, denoted by an overbar, and the deviations therefrom, denoted by a prime, such that for any quantity A, we have $A = \overline{A} + A'$. So, $\overline{u}$ is the zonal-mean zonal wind, and $\overline{X}$ represents the zonal-mean frictional drag (if any). In the above equation, $\overline{v}^*$ and $\overline{\omega}^*$ give the "residual-mean" meridional and vertical velocities, respectively, which typically provide a much better approximation of the Lagrangian-mean circulation and tracer transport than do the conventional Eulerian-mean velocities $\overline{v}$ and $\overline{\omega}$ (e.g., Andrews et al. 1987). In the above equation, the zonal acceleration of the zonal-mean flow caused

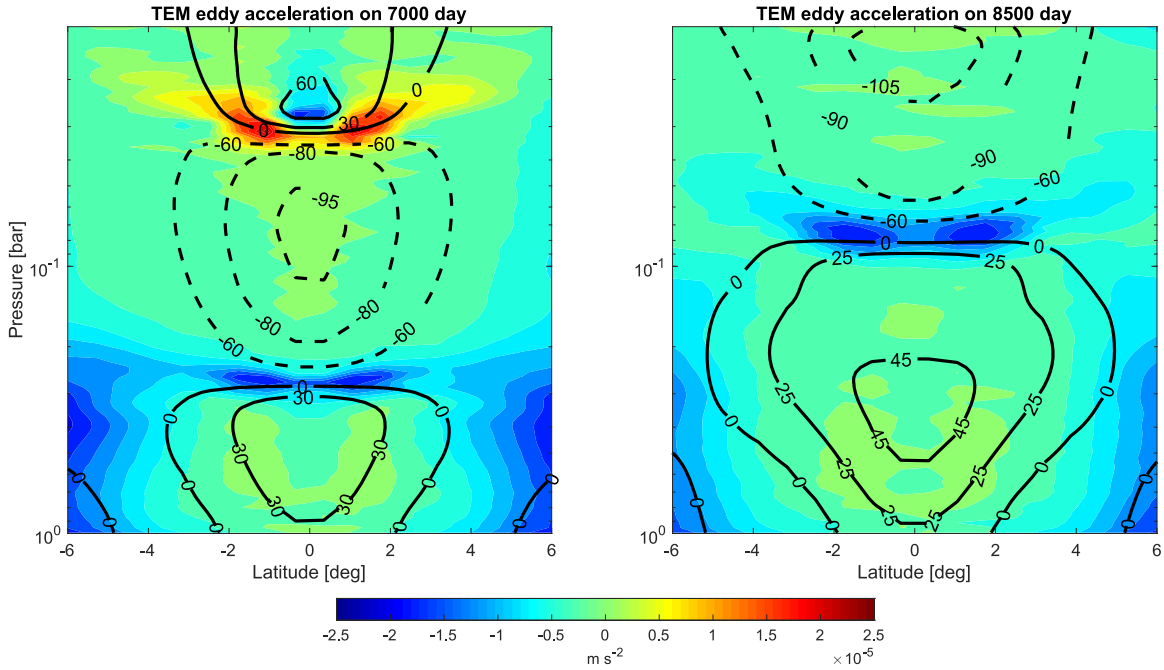

Figure 11. Zonal-mean wave-induced acceleration (colorscale, m s^{-2}) vs. latitude and pressure at two times during the cycle of a QBO-like oscillation, at 7000 and 8500 days on the left and right, respectively. Zonal-mean zonal wind is depicted in thick black contours (labeled in m s^{-1}); eastward is positive (solid) and westward is negative (dashed). Note that the wave-induced accelerations of a given sign occur primarily near the base of the zonal jet of that same sign—specifically, at both times, the waves induce westward acceleration near the base of the westward jet and eastward acceleration near the base of the eastward jet. This has the effect of causing the jet to migrate downward over time and indicates that the QBO-like oscillation is wave-driven. This is the same model as shown in the top row of Figure 6.

by waves is given by the divergence of the Eliassen-Palm flux $\boldsymbol{F}$ in the meridional plane.[8]

Our results show that, at low latitudes, the wave driving induces vertically stacked layers of eastward and westward acceleration, with the peak accelerations shifted downward from the peak of the zonal jet, in just the manner required to cause a QBO-like oscillation. Figure 11 illustrates this phenomenon; it shows meridional cross sections of the zonal-mean zonal wind (thick black contours) and Eliassen-Palm flux divergence (colorscale) versus latitude and pressure at two different phases of the oscillation, at 7000 and 8500 Earth days (the long-term evolution of the equatorial-jet structure for this same model can be seen in Figure 9). At both timeframes, the peak eastward acceleration caused by the waves occurs on the lower flank of the eastward equatorial jet, whereas the peak westward acceleration caused by the waves occurs on the lower flank of the westward equatorial jet. At 7000 days (Figure 11, left), the zonal jet structure comprises an eastward jet extending from ∼1 to ∼0.3 bar, a westward jet from 0.3 to 0.03 bar, and then an eastward jet from 0.03 bar to the top of the model. Strong westward acceleration occurs in a layer between 0.2 and 0.3 bars—at the base of the westward jet—and strong eastward acceleration occurs in a layer near 0.03 bars—at the base of the uppermost eastward jet. At 8500 days, the uppermost eastward jet has migrated downward to the bottom of the model; its top reaches ∼0.08 bars, above which is a newly formed westward jet that extends from 0.08 bars to the top of the model. At this time, strong westward acceleration occurs right at the base of the westward jet at a pressure of ∼0.06–0.08 bars. As described earlier, this basic acceleration pattern—namely that the peak accelerations of a given sign occur primarily near the base of the zonal jet of that same sign—causes the zonal jets to migrate downward over time. Figure 11 demonstrates that this acceleration is caused by waves.

We next turn to characterize the types of waves that are relevant, starting with an examination of the wave spatial structure. Figure 12(a) shows a snapshot of the wave perturbations versus longitude and pressure in the equatorial plane. Many superposed modes are present, including waves whose phases tilt upward to the east and waves whose phases tilt upward to the west. A count of wave crests and troughs suggests that modes exhibiting zonal wavenumbers $k \sim 10$–20 are prominent. Moreover, the character of the waves changes significantly with altitude, suggesting a strong interaction between the waves and the background zonal flow. This snapshot is at 7000 Earth days in the same model discussed previously, with eastward jets at the top and bottom and a westward jet in between, and there are strong transitions in the wave structure at pressures of ∼0.2–0.3 bars and ∼0.03 bars, exactly where the zonal jet changes sign. The phase tilts evident in Figure 12(a) suggest the existence of Kelvin waves, which exhibit phase tilting upward to the east, as well as equatorially trapped Rossby and/or MRG waves, which exhibit phase tilting upward to the west (see phase relations in Andrews et al. (1987)). The waves attain velocity amplitudes of tens of m s^{-1} or more—which approaches the zonal-mean

[8] In pressure coordinates on the sphere, the Eliassen-Palm flux, $\boldsymbol{F} = (F_\phi, F_p)$, is (e.g., Andrews et al. 1983)

$$\boldsymbol{F} = a\cos\phi\left\{-\overline{u'v'} + \frac{\overline{v'\theta'}}{\partial\overline{\theta}/\partial p}\frac{\partial\overline{u}}{\partial p}, \right.$$
$$\left. -\overline{u'\omega'} - \frac{\overline{v'\theta'}}{\partial\overline{\theta}/\partial p}\left[\frac{1}{a\cos\phi}\frac{\partial(\overline{u}\cos\phi)}{\partial\phi} - f\right]\right\} \quad (10)$$

and the divergence of $\boldsymbol{F}$ is

$$\nabla\cdot\boldsymbol{F} = \frac{1}{a\cos\phi}\frac{\partial(F_\phi\cos\phi)}{\partial\phi} + \frac{\partial F_p}{\partial p}. \quad (11)$$

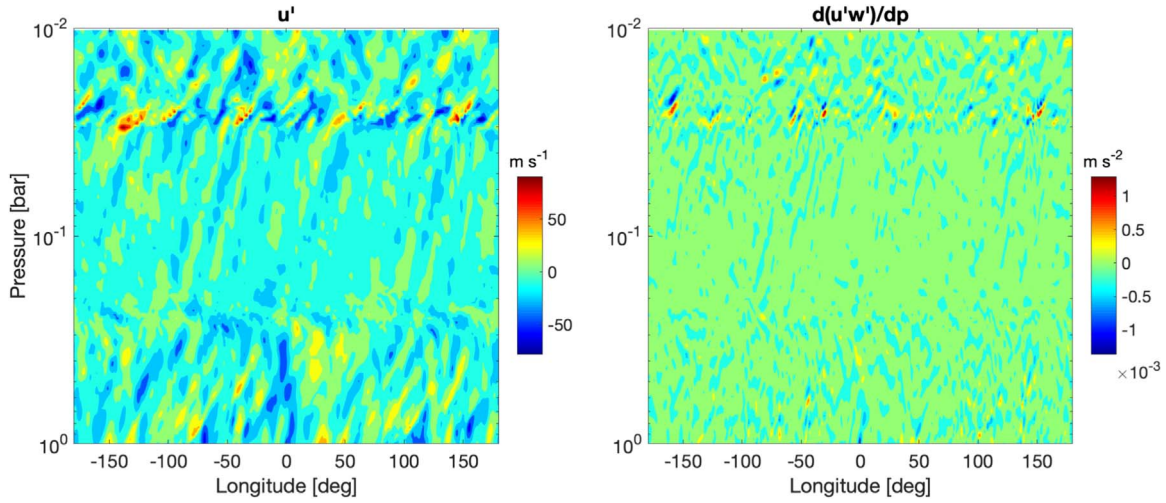

Figure 12. Spatial structure of typical waves at the equator in a simulation generating a QBO-like oscillation. (a) Zonal wind anomalies u' in m s^{-1} (that is, deviations of zonal wind from the zonal mean at that pressure) shown at the equator vs. longitude and pressure. Waves of typical zonal wavenumber ∼10–20 can be seen, tilting both upward to the right and upward to the left, reminiscent of Kelvin waves and equatorially trapped Rossby and/or mixed Rossby-gravity waves, respectively. The wave structure undergoes transitions at ∼0.2–0.3 and 0.03 bars where the zonal-mean zonal wind changes sign. Although this shows perturbations of zonal wind u', the patterns look qualitatively similar in v' and T'. (b) The wave-induced acceleration $\partial(u'\omega')/\partial p$, which is one component of the EP flux divergence, again shown vs. longitude and pressure at the equator. The accelerations are strongest at a pressure ∼0.03 bars, near the transition between an eastward jet above and a westward jet below. Both panels are snapshots at 7000 days in the same model shown in Figure 11.

zonal wind speeds (Figure 11). This fact suggests that the wave–mean-flow interactions are probably not in a regime where the waves can be considered small perturbations relative to the mean flow. Figure 12(b) shows the structure of the term $\partial(u'\omega')/\partial p$, which is one component of the EP flux divergence. Consistent with Figure 11(a), its peak values occur at a pressure of ∼0.03 bars; here, however, no zonal mean has been performed, and we can see that the acceleration varies longitudinally in a highly patchy manner, consistent with wave acceleration being caused by the absorption of local wave packets as they reach their critical levels.

Hovmöller diagrams confirm the existence of both eastward- and westward-propagating wave modes, constrain their phase speeds, and show that the wave population changes significantly with altitude. Figure 13 presents such diagrams—specifically, temperature anomalies T' versus longitude and time are shown at three different pressure levels at the equator over a 70 day interval starting at 7000 days. The equatorial jet structure at this time comprises a vertically stacked structure with an eastward jet at the bottom, a westward jet in the middle, and another eastward jet at the top (see Figure 11(a)), and Figure 13 shows Hovmöller diagrams plotted within these three jets, at 0.3, 0.04, and 0.02 bars, respectively.

In Figure 13, eastward-propagating modes tilt upward to the right, while westward-propagating modes tilt upward to the left. Both types of modes are prominent at 0.3 bars (Figure 13, bottom panel), which is inside the lowermost eastward jet associated with the oscillation. The eastward-propagating modes circumnavigate the planet's circumference in ∼50 days, implying a phase speed of about 100 m s^{-1} eastward. At least two classes of westward-propagating modes are evident. A slow westward-propagating component is most prominent, and travels about 100° longitude in the 70 day interval, implying a phase speed of −20 m s^{-1} westward. A faster, less-prominent component traverses the planetary circumference in about 25–30 days, implying phase speeds approaching −200 m s^{-1}. Moving upward into the westward jet at 0.04 bars (Figure 13, middle), the eastward-propagating modes still exist. However, a key point is that the slowly propagating westward-propagating modes are now absent. The top panel, at 0.02 bars, is similar—lacking the slow westward-propagating modes yet still retaining the eastward-propagating component. The most prominent eastward-propagating modes now traverse the planet's circumference in about 40 days, implying a speed of about 130 m s^{-1}. Because the westward jet attains peak speeds of −90 m s^{-1}—which exceeds the phase speeds of the prominent, slowly propagating westward-propagating modes seen in Figure 13, bottom—the implication is that those modes have encountered a critical level and been absorbed, explaining their absence in the top two panels of Figure 13. The change in speed of the eastward-propagating modes between the middle and top panels suggests either that the wave properties change with altitude or that the slower of the eastward-propagating modes have been removed, leaving the faster waves behind. The fast-westward-propagating modes (mentioned above) exist not only at 0.3 bars but at 0.04 and 0.02 bars as well (Figure 13, middle and top); because the phase speeds of these waves exceed the wind speed of the westward jet, these waves do not encounter critical levels, and thus it makes sense that they would be present at all levels shown. The key takeaway point is that the wave properties presented in Figure 13—particularly the loss of the slow westward-propagating component between the bottom and middle panels—match expectations for the QBO-driving mechanism described in the preceding subsection.

Additional insight into the wave properties can be obtained by performing a spectral analysis at the equator in the wavenumber-frequency domain, similar to that performed by Wheeler & Kiladis (1999). To do so, we first obtain the eddy terms as a function of longitude and time at the equator and at a given pressure level. We do the analysis using eddy temperatures, though qualitatively similar results would be expected for other eddy components as well. We then perform two-dimensional fast Fourier transforms on the data set, to obtain the raw Fourier coefficients in the wavenumber-frequency space. Next, we

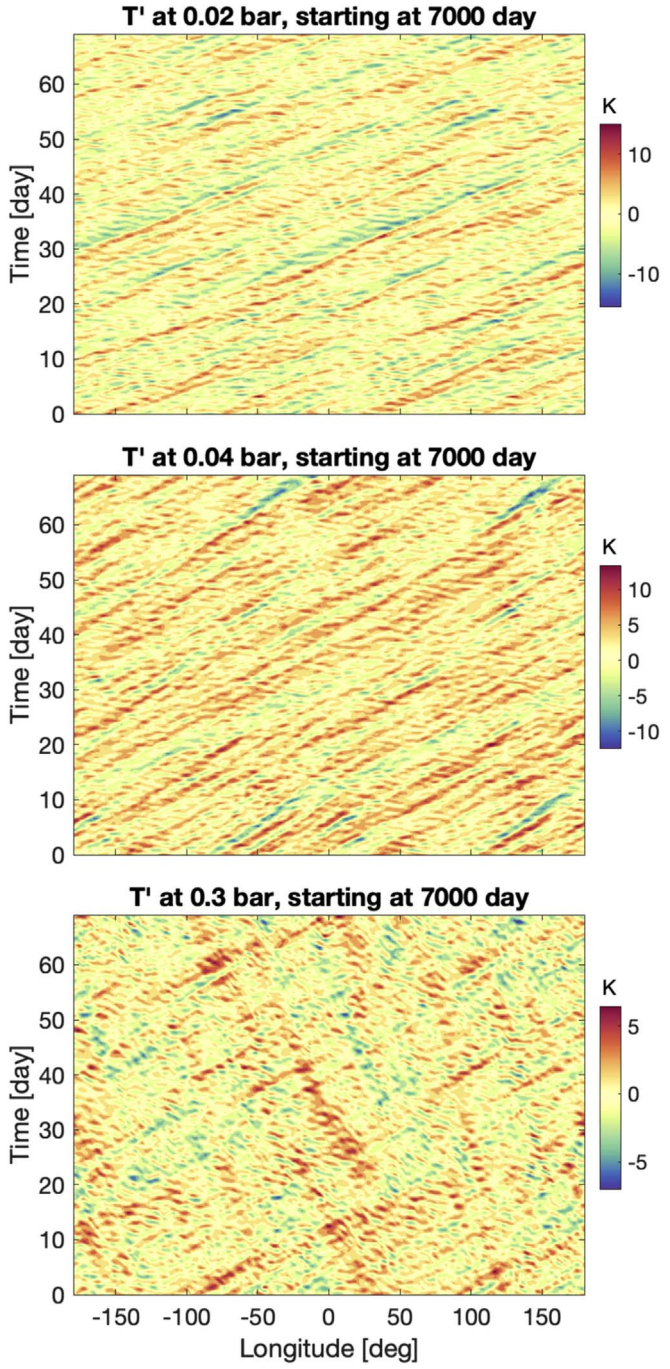

Figure 13. Hovmöller diagrams showing the time evolution of temperature anomalies at the equator (that is, local temperature minus the zonal mean, in K) over a 70 day interval at 7000 days in a model exhibiting a QBO-like oscillation. Pressure levels of 0.3, 0.04, and 0.02 bars are shown, lying within vertically stacked eastward, westward, and eastward equatorial jets, respectively (see Figure 11, left, for the zonal jet structure at this time). Both eastward- and westward-propagating modes can be seen within the lowermost eastward jet (0.3 bars), but the most prominent slow westward-propagating modes have been filtered out at 0.04 and 0.02 bars, suggesting absorption of these waves at critical levels. This is the same model shown in Figure 6 (top row), 7–9.

perform smoothing by applying 40 iterations of the so-called 1-2-1 filter in wavenumber and frequency to the raw coefficients, after which we get a background spectrum. Finally, we apply the 1-2-1 filter once to the raw coefficients in wavenumber and frequency, and then divide by the background spectrum. What we ultimately obtain is the relative power of the coefficients in frequency-wavenumber space. Significant signals will appear to have values greater than 1. Note that we have performed the analysis on the full eddy field, rather than separating it into symmetric and antisymmetric components about the equator as done by Wheeler & Kiladis (1999). The final spectra are plotted in Figure 14. As is standard practice, the frequency is plotted in cycles per day (thus, to obtain the angular frequency, multiply the frequencies by 2π).

Our wavenumber-frequency spectra demonstrate the existence of Kelvin waves, equatorially trapped Rossby waves, and MRG waves, and indicate that some of these modes are preferentially absorbed with height. Figure 14 shows such wavenumber-frequency spectra for the same three pressure levels and same time as shown in Figure 13. In the diagrams, positive wavenumbers correspond to eastward phase propagation while negative wavenumbers represent westward phase propagation. Analytic dispersion relations for relevant equatorial waves are overplotted (e.g., Andrews et al. 1987), and are labeled in the figure. A brief summary of the primary modes identifiable in our frequency-wavenumber diagrams is as follows:

1. *Kelvin waves:* the Kelvin wave branch is comprised of straight lines extending from the origin upward to the right, exhibiting only eastward phase speeds. The highest-amplitude Kelvin waves present in our model exhibit zonal wavenumbers of 20, but high-amplitude Kelvin modes also exist at wavenumbers ∼2–13, and lower-amplitude Kelvin modes manifest across a range of other wavenumbers. Multiple branches of Kelvin waves are visible, likely due to the presence of a range of vertical wave lengths, which would lead to a range of frequencies and phase speeds for a given zonal wavenumber. Phase speeds ω/k range from 90 to 200 m s^{-1}. Some of the modes are present at all three pressure levels, particularly the faster modes (e.g., the mode at 0.8 CPD and $k = 20$), but it appears that the slower modes are only present at the deepest levels.
2. *Rossby waves:* Rossby waves lie at low frequencies to the left of the origin, exhibiting only westward phase speeds (Figure 14, bottom panel). Rossby wave amplitudes are strongest for zonal wavenumbers of ∼3–20, though such modes can be identified at wavenumbers as high as 40. Phase speeds calculated for the largest-amplitude Rossby waves in Figure 14 range from −20 to −40 m s^{-1}. Crucially, the Rossby waves only exist in the bottom panel of Figure 14, suggesting that they have been absorbed before they can propagate to the pressures shown in the top two panels. As mentioned previously, at the time of this snapshot, any westward-propagating wave with a phase speed amplitude between 0 and −90 m s^{-1} will encounter a critical level before reaching the middle or upper panel of Figure 14.
3. *MRG waves:* interestingly, the analysis also indicates the presence of the MRG at the deepest levels. In principle, the MRG can exhibit either eastward or westward phase speeds, but the MRG modes with the strongest amplitudes in our model are westward and exhibit zonal wavenumbers between ∼1 and 40 (Figure 14, bottom panel). The phase speeds for the most prominent modes exhibit a wide range, from −20 to nearly −400 m s^{-1}. Just as for Rossby waves, most of these MRG modes, particularly the ones with slower phase speeds, are absent at lower pressures (upper

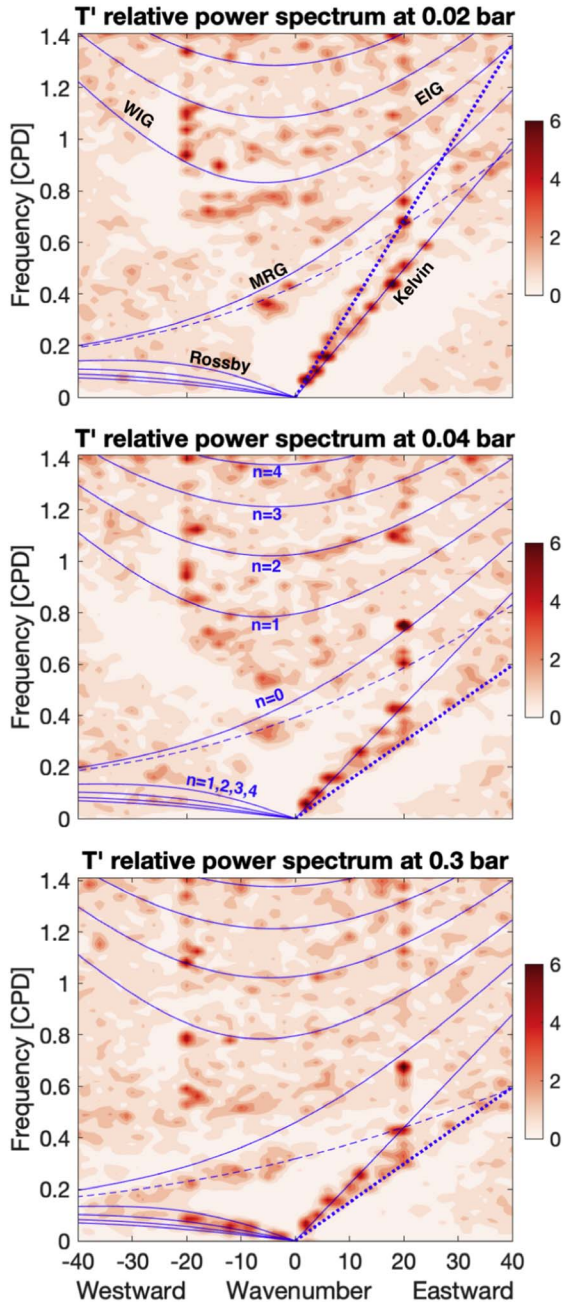

Figure 14. Wavenumber-frequency spectra (Wheeler–Kiladis diagrams) at 7000 days in a model exhibiting a QBO-like oscillation. Pressure levels of 0.3, 0.04, and 0.02 bars are shown, lying within vertically stacked eastward, westward, and eastward equatorial jets, respectively. Abscissa gives the zonal wavenumber; positive and negative represent eastward and westward propagating waves, respectively. Ordinate is frequency in cycles per day (CPD). Colorscale indicates wave power density; darker red coloration indicates that waves with significant power exist at that wavenumber and frequency. Curves indicate theoretical dispersion relations for various wave types: Kelvin waves, equatorially trapped Rossby waves, mixed Rossy-gravity (MRG) waves, and eastward and westward inertio-gravity waves (EIG and WIG, respectively) are all shown. Equivalent depths are chosen to be broadly illustrative of the types of waves seen; no attempt has been made to fit the theoretical curves to the power densities. In the upper panel, the solid lines all correspond to $h_e = 33$ m, the dotted line is a Kelvin mode with $h_e = 63$ m, and the dashed line is an MRG mode with $h_e = 20$ m. In the middle panel, the corresponding three values are 26, 12, and 14 m, respectively, while in the bottom panel they are 26, 12, and 6 m, respectively.

two panels of Figure 14). Again, this is consistent with their loss via absorption at critical levels encountered at the base of the westward equatorial jet.

4. *Inertio-gravity waves:* finally, the analysis indicates the presence of fast inertio-gravity waves propagating both east and west. Figure 14 shows that the power in these IG modes remains focused at wavenumbers comparable to the forcing wavenumber ($k = 20$), suggesting that nonlinear interactions are too weak to cause significant transfer of power to other wavenumbers (unlike the Kelvin, Rossby, and MRG waves, where the presence of power over a broad range of wavenumbers suggests that such interactions are important). Nevertheless, the frequencies of the most prominent IG modes exhibit modest changes as a function of altitude, suggesting possible effects of the stratification and/or the background mean flow. The phase speeds for the dominant IG modes in Figure 14 are fast, exceeding an amplitude of 200 m s^{-1}, so no critical level absorption is expected; this is consistent with the fact that these wave modes exist at all three levels shown.

In summary, this Wheeler–Kiladis analysis indicates that the convective forcing generates a wide range of equatorially trapped waves, and that some of these wave modes disappear at progressively higher altitudes, in a manner consistent with critical level absorption.

To seek "smoking gun" evidence for the role of waves in driving the QBO-like oscillation, we now calculate the phase speed spectra of the wave modes present near the equator, and show how these phase speed spectra vary with pressure. To analyze the eddy flux (for example $u'\omega'$) in ω–k space, we need to do cross spectral analysis. The basic procedure is analogous to that described in Randel & Held (1991). First, we calculate the cross-spectral power density (CSPD) in ω–k space for propagating atmospheric waves following the method laid out by Hayashi (1971). This is done for all relevant eddy flux including $u'\omega'$, $u'v'$, and $v'T'$. Next, we convert the CSPD to wavenumber–phase-speed space following Randel & Held (1991). The Eliassen-Palm flux in wavenumber-phasespeed space is calculated by multiplying the constant coefficients and grouping all relevant terms as shown in Equation (10). The TEM eddy acceleration in wavenumber-phasespeed space is calculated by taking the appropriate derivatives as in Equation (11). Finally, the TEM eddy acceleration in the phasespeed domain is calculated by integrating the function over the wavenumber domain.

Figure 15 shows the resulting phase-speed spectra versus pressure for the same two timeframes during a QBO-like oscillation as are shown in Figure 11—namely, 7000 and 8500 days, on the left and right, respectively. Let us first examine the top row, which shows the phase-speed spectra of the vertical component of the Eliassen-Palm flux. At any given pressure, the amplitudes at various wavenumbers represent a spectrum giving the range of zonal phase speeds exhibited by the waves (with the plotted amplitudes normalized by the maximum value at that pressure), and comparing different pressures shows how the mode population varies with altitude. The thick dashed curve shows the zonal-mean zonal wind at the time of this analysis. At both time intervals, the deepest regions shown exhibit prominent waves with westward phase speeds ranging from -10 to -180 m s^{-1} and eastward phase speeds from 50 to 150 m s^{-1}. At 7000 days, it can be seen that the modes with westward phase speeds continue until they reach pressures of ~0.2–0.3 bars, above which they disappear. At 8500 days, the pattern is similar, except that the westward-propagating modes reach pressures as low as 0.06–0.07 before they disappear. It is

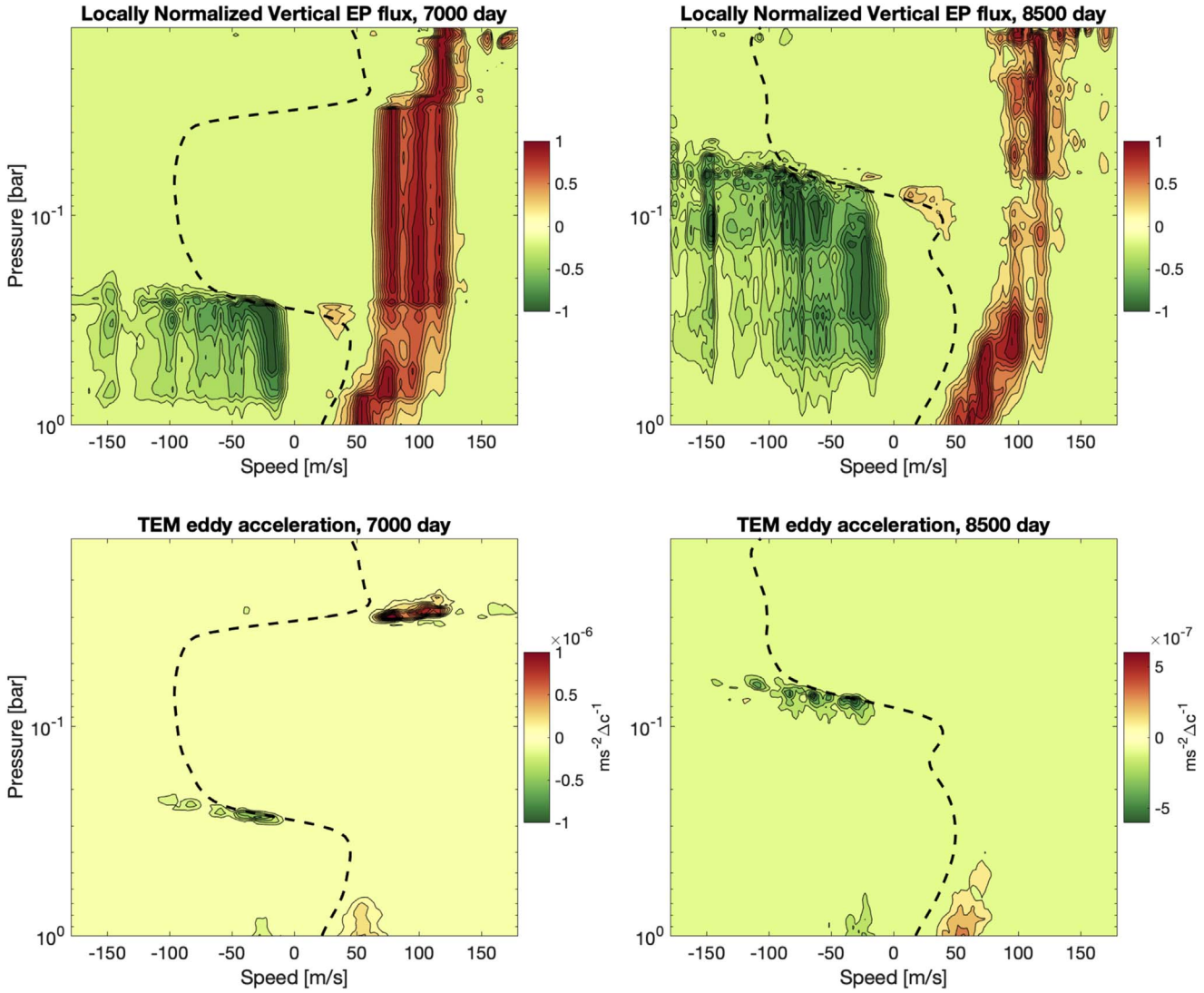

Figure 15. Phase-speed spectra of the Eliassen-Palm flux (top) and Eliassen-Palm flux divergence (bottom) at 7000 and 8500 Earth days on the left and right, respectively, showing the absorption of waves at critical levels in a model with a QBO-like oscillation. The equatorial zonal-mean zonal wind profiles at the corresponding times are overplotted in thick dashed curves. In the top panels, the spectra are of the vertical component of the Eliassen-Palm flux vector, and the spectra are normalized at every pressure by the maximum value at that pressure. The spectra comprise eastward-propagating modes with speeds of 50 to $\sim$140 m s^{-1} and westward-propagating modes with speeds of about -10 to -150 m s^{-1}, which propagate upward from near the bottom (pressures of around a bar). The westward-propagating modes shown here (which, as shown in Figure 14, are primarily Rossby and mixed Rossby-gravity waves) are absorbed near a critical level when they reach the base of the westward zonal jet (at 0.02–0.03 bars at 7000 days, and $\sim$0.06–0.08 bars at 8500 days). Some of the eastward-propagating modes (which, as shown in Figure 14, are primarily Kelvin waves) are absorbed at critical levels, though some of them are able to propagate upward throughout the plotted region without being absorbed. The bottom panels show that the zonal accelerations caused by the wave absorption are eastward (orange/red colors) on the lower flank of the eastward jet, and westward (green) on the lower flank of the westward jet, as necessary to cause the downward zonal-jet migration occurring in the QBO-like oscillation. This figure provides strong evidence that the QBO-like oscillation in the numerical experiment is driven by critical-level absorption of vertically propagating atmospheric waves, as described in the text.

clear that many of these westward-propagating waves have reached a critical level, because their amplitude sharply decreases with altitude at precisely the altitude where their zonal phase speed matches that of the zonal-mean zonal wind. These waves are primarily Rossby and MRG waves, as Figure 14 makes clear. Considering now the eastward-propagating modes, the slowest modes (phase speeds $\lesssim$60 m s^{-1}) disappear at pressures less than $\sim$0.3 bars. At 7000 days, Kelvin waves with eastward phase speeds of 70–100 m s^{-1} disappear on the lower flank of the eastward jet (although the Kelvin wave with phase speed $\sim$120 m s^{-1} continues unimpeded to the top of the plot). In contrast, at 8500 days, there is no strong eastward jet at the top of the model, and most of the fast Kelvin waves propagate upward unimpeded.

The bottom row of Figure 15 shows the phasespeed spectra of the TEM acceleration versus pressure. Essentially, this is just a decomposition of $\nabla \cdot \boldsymbol{F}$ (see Equation (9)) showing the phase speeds of the waves that contribute to the TEM acceleration; positive values indicate an eastward acceleration and negative values indicate a westward acceleration. It can be seen that absorption of westward-propagating waves near the critical levels at the base of the westward jet causes westward acceleration, while the absorption of eastward-propagating waves on the critical level near the base of the eastward jet

causes eastward acceleration. These zonal accelerations caused by critical-level absorption are just those shown in Figure 11, and are responsible for the downward migration of the QBO-like oscillation in our experiments.

To summarize, Figure 15 provides decisive evidence that the wave-driving mechanism, as understood for the terrestrial QBO and as outlined in the preceding subsection, causes the QBO-like oscillations in our models.

Nevertheless, a puzzling aspect emerging from Figure 15 is that some of the westward-propagating waves absorbed on the lower flank of the westward jet, as well as some of the eastward-propagating waves absorbed on the lower flank of the eastward jet, have phase speeds *faster* than those of the zonal-mean zonal wind, implying that they do not appear to have reached critical levels.[9] Stated another way, Figure 15 seems to indicate that the waves *act* as if they have reached critical levels for a zonal-mean zonal-wind profile that is *faster* than the actual zonal-mean zonal-wind profile. This behavior is not predicted by classical wave–mean-flow interaction theory, which applies to small amplitude waves and adopts the WKB approximation, under which the background zonal-flow properties change over length scales that are long compared to the vertical wavelength of the waves.

We suggest two hypotheses that could potentially explain the unexpected nature of the critical-level dynamics in our simulations. First, the WKB approximation is not well-satisifed in our models; the wavelengths of the convectively generated waves in our models are not generally short compared to the vertical scale over which the zonal wind varies (compare the wave vertical wavelengths in Figure 12 with the zonal-mean zonal wind structure in Figures 11 and 15). We speculate that this effect could change the nature of the wave–mean-flow interactions, perhaps helping to explain the behavior seen in Figure 15. The second hypothesis is that the phenomenon results from a nonlinearity associated with the large wave amplitudes: as mentioned previously and shown in Figure 12, the local wave amplitudes u' attain speeds approaching that of the local zonal flow, and thus quasi-linear wave–mean-flow interaction theory may not apply. While the precise mechanism remains to be investigated, we speculate that the large wave amplitude causes the wave to "sense" an effective zonal-jet speed greater than the actual value of $\overline{u}$. For example, Figure 12 indicates that the wave amplitudes at 0.03 bars—where many eastward-propagating waves are absorbed—are 50 m s^{-1} at most longitudes, and reach twice this value in a few local regions. This level and time correspond to the base of an eastward jet whose zonal-mean zonal wind speeds $\overline{u}$ reach 50 m s^{-1} (Figure 15, left). This implies that, *locally*, at the longitudes where the wave anomalies are eastward, the zonal wind reaches speeds up to 150 m s^{-1}. We speculate, then, that the waves of phase speeds 70–100 m s^{-1} (which Figure 15 indicates are absorbed) act as though they are reaching a critical level, due to the fact that the local zonal wind speed at certain longitudes matches the wave's phase speed—even though the *zonal-mean* zonal wind never reaches such high values. Detailed investigation of this hypothesis and other aspects are left for the future.

[9] At 7000 days, this is particularly true for westward-propagating waves with phase speed amplitudes faster than 90 m s^{-1} at ∼0.3 bars, and for eastward-propagating waves with speeds of 70–100 m s^{-1} at ∼0.03 bars. At 8500 days, it is primarily true for westward-propagating waves of speeds exceeding 100 m s^{-1} at ∼0.06 bars, and eastward-propagating modes of speeds ∼70–80 m s^{-1} that are absorbed near 0.3 bars.

3.5. Implications for Jupiter and Saturn

Our idealized model with isotropically imposed thermal perturbations holds promise for understanding the general circulation of Jupiter and Saturn. In particular, some of our models exhibit zonal-jet structures very similar to those on Jupiter and Saturn, including multiple off-equatorial (mid-to-high latitude) zonal jets and a broad, stable, equatorial eastward jet—i.e., equatorial superrotation. Figure 5 illustrates an example, showing the zonal wind and vorticity at 1.5 bars pressure, which is in the troposphere, deeper than the level where the QBO-type oscillations occur. Thus, the equatorial superrotation shown in Figure 5 is a stable, long-term feature, in contrast to the oscillating eastward and westward jets seen in the QBO-type oscillations in other models. In Figure 5, the zonal-wind speed in the mid-to-high-latitude and equatorial jets reach 50–100 m^{-1} and ∼300 m s^{-1}, respectively. These speeds are intermediate between the jet speeds on Jupiter and Saturn, though closer to the latter. Although the equatorial jet in this model is a stable feature, even in this model, there exists—at lower pressure, at ∼0.02–1 bar, within the model's stratosphere and upper troposphere—a QBO-type oscillation *within* this robust equatorial superrotation, in a way similar to how the QQO and SAO on Jupiter and Saturn represent stratospheric perturbations around a long-lived, stable equatorial superrotating jet that is rooted in the troposphere.

Although the zonal jets in this model are rather zonally symmetric at low latitudes, they experience greater meanders at high latitudes, which resemble a large-scale, polygonal structure when viewed from over the pole (Figure 4, upper right panel; a quasi-hexagonal structure can be seen in the yellow, circumpolar ring of postive relative vorticity at ∼65–70° latitude). This feature is similar to—and relevant for understanding—the polar hexagon in Saturn's northern hemisphere (e.g., Baines et al. 2009; Morales-Juberías et al. 2015). The hexagonal pattern seen in Figure 4 represents equatorward/poleward deflections of the prominent zonal jet at ∼65°, which is the closest eastward zonal jet to the pole in this model (see Figure 5(a)). Nevertheless, the hexagonal structure in this simulation is less prominent than Saturn's hexagon, both in that the vertices are not as sharp and that the sides are not all equal in length. The hexagon on Saturn is also at higher latitude (∼76°) than that shown here—presumably a simple result of the latitude at which the most poleward jet occurs. Within the hexagon, there exist several cyclonic and anticyclonic vortices as well as turbulent filaments likely associated with vorticity mixing. Further studies of the properties of such polar polygons in this class of model would be useful.

The QBO-type oscillations in the models shown in this paper exhibit periods that bracket those observed on in the Jovian QQO and Saturnian SAO. The QBO-type oscillations for the two simulations in Figure 6 exhibit periods of 12 and 19 yr, bracketing the 15 yr period for Saturn's SAO (Fouchet et al. 2008; Orton et al. 2008; Guerlet et al. 2011). The QBO-type oscillation for the model in Figure 5 has a period of ∼400–500 days, which is several times shorter than that of Jupiter's QQO.

A detailed comparison of the QBO-like oscillations in our models to Jupiter's QQO and Saturn's SAO reveals similarities and differences. The observed temperature anomalies on both planets exhibit temperature extrema at the equator that are anticorrelated with those immediately north and south (Guerlet et al. 2011; Fletcher et al. 2016; Cosentino et al. 2017; Guerlet et al. 2018), a feature also shared by our simulations (Figure 8).

The temperature anomalies observed on Jupiter exhibit amplitudes of order ±5 K, similar to those in our model depicted in Figure 8, whereas the temperature anomalies of Saturn's SAO are roughly twice as large, about ±10 K. A significant discrepancy between our models and the actual QQO and SAO is that the temperature anomalies (including both the central temperature extrema at the equator and the anticorrelated extrema on either side) extend to latitude 20–25° on Jupiter and Saturn but only to 15° in our models (Figure 8). This difference probably results in large part from the faster rotation rates of our models, which confines the equatorial waveguide closer to the equator. The equatorial Rossby deformation radius—which represents the half-width of the waveguide—is $L_{\rm eq} = \sqrt{NH/\beta}$. Our models adopt a rotation rate twice that of Jupiter. Everything else being equal, this implies an equatorial deformation radius 70% that on Jupiter, and should lead to equatorial oscillations with a meridional width that is narrower by a similar factor.

Another significant difference from Jupiter and Saturn is that the QBO-like oscillations in our models occur at greater pressures than Jupiter's QQO and especially Saturn's SAO. In our model, the oscillation occurs primarily between 1 bar and the top of the model at 10 mbar. The QQO extends from ~1 to 100 mbar (Fletcher et al. 2016; Cosentino et al. 2017) while the Saturn SAO occurs primarily between 0.01 and 10 mbar. An obvious future step would be to extend the model top to lower pressures and investigate whether the additional "room" promotes a natural extention of the oscillation to lower pressures. One also expects the oscillation to be affected by the vertical stratification profile. The greater gravities of brown dwarfs shift the tropopause (defined here as the deepest level where the stratification becomes significant) to deeper pressures than on Jupiter and Saturn,[10] and this fact motivated our choice of background temperature profile (Figure 1). We speculate that a model whose background temperature profile is chosen to match that of Jupiter or Saturn may naturally exhibit oscillations that are shifted to lower pressures. Regardless, the question of what controls the vertical pressure range over which the oscillation occurs—and the extent to which the modeled range matches that observed on Jupiter and Saturn—is a critical question that needs to be addressed in future models.

Although we have captured many elements of the circulations on Jupiter and Saturn in some simulations—numerous east–west zonal jets, equatorial superrotation, stratospheric QQO and SAO-type oscillations, and tendencies toward polar polygons—our overall emphasis has been on understanding the overall dynamical behavior across a wide range of conditions relevant to giant planets and brown dwarfs generally. As such, we have not attempted to "tune" models to match precisely the observed properties of Jupiter and Saturn. It would be valuable to perform follow-on studies aimed at determining the conditions under which the particular details of the circulations on these planets—jet speeds and profiles, temperature perturbations, and the periods, amplitudes, and meridional structure of the QQO and SAO—can be matched.

[10] For a constant specific absorption coefficient $k_{\rm abs}$ in the IR, one expects the pressure at optical-depth unity to be approximately $g/k_{\rm abs}$. Because the tropopause usually occurs near this level, one expects the tropopause pressure to scale with gravity in a similar manner. A typical brown dwarf has a gravity dozens of times larger than Jupiter's, and thus can have a tropopause that is much deeper than on Jupiter and Saturn.

In the context of the present simulations, the temperature profile primarily exerts an influence via the height-dependence of the Brunt–Vaisala frequency that it implies, rather than via the absolute temperature itself.[11] We thus might expect that otherwise similar simulations that replace the temperature profile in Figure 1 with one more appropriate for Jupiter or Saturn would yield qualitatively similar results. To test this, we performed a few simulations where we adopted a temperature profile similar to that observed on Jupiter, with an isothermal temperature $T_{\rm iso} = 110$ K at the top, transitioning to an adiabatic temperature profile with a constant potential temperature of $\theta_{\rm ad} = 165$ K in the interior. We also lessened the forcing amplitude in these models to be more appropriate for the cooler temperatures. As expected, these models produce behavior qualitatively similar to that described in Sections 3.1–3.3, including the generation of multiple zonal jets, as well as QBO- or QQO-like oscillations in some models. We defer a focused investigation in the exact parameter regime of Jupiter and Saturn to the future.

4. Conclusions and Discussion

We have presented idealized 3D simulations of brown dwarfs and Jupiter- and Saturn-like giant planets to test the hypothesis that interaction of convection with an overlying stratified atmosphere can lead to a vigorous atmospheric circulation consisting of zonal jets and turbulence, long-term variability, and stratospheric oscillations. We have also sought to ascertain how the properties of the circulation vary over a wide range of parameters relevant to brown dwarfs and Jupiter-like planets. Convection was parameterized by introducing small-scale, random, horizontally isotropic thermal perturbations near the bottom of the domain, which represent the effect of convective plumes in perturbing the RCB at the base of the atmosphere.

Our primary results are as follows:

1. We showed that, under the rapidly rotating conditions relevant to brown dwarfs and Jupiter-like planets, zonal jets are a robust, ubiquitous outcome of the dynamics. Under forcing and damping conditions relevant to brown dwarfs and giant planets, wind speeds typically range from tens to hundreds of m s^{-1} and horizontal temperature perturbations on isobars are typically several to tens of K. These ranges agree with the wind speeds and temperature perturbation amplitudes predicted in an analytical scaling theory by Showman & Kaspi (2013). As expected, stronger forcing leads to stronger jets, while stronger radiative and/or frictional damping leads to weaker jets. Generally, for similar wind speeds, models with weak forcing and damping exhibit a more zonally symmetric pattern than models with strong forcing and damping. In models with strong jet formation, the PV tends to be homogenized in strips, leading to a staircase pattern of PV with latitude.
2. Our simulations show that, under conditions of weak radiative and frictional damping, the zonally banded pattern—and zonal jets—occur over a wide latitude range from the equator to near the poles. When the radiative or frictional damping are strong, however, the zonal banding

[11] The radiative time constant strongly affects the results, of course, but this is an independent parameter in our setup.

becomes confined to low latitudes, with the higher latitudes dominated primarily by wave dynamics. This behavior naturally results from the fact that the ability of the convective perturbations to generate jets is stronger near the equator and weaker near the poles, due to a combination of factors, including the latitudinal variation of both the β effect and the ability of the convective perturbations to generate Rossby waves, which are critical in jet formation.

3. Under appropriate conditions, our models produce long-term oscillations in the stratospheric jet structure, in which vertically stacked eastward and westward zonal jets migrate downward, analogous to the terrestrial QBO, Jovian QQO, and Saturnian SAO. Our simulations are the first demonstration of a QBO-like oscillation in full 3D numerical simulations a giant planet. The ranges of periods and other properties seen in our oscillations are similar to, and bracket, those of the observed QQO and SAO. The possibility of such phenomena on brown dwarfs suggests the possibility of very long-term (multi-annual) variability, which could be monitored in long-term ground-based surveys.
4. Detailed diagnostics show that the convective forcing drives a broad population of equatorial waves, including Kelvin, Rossby, MRG, and inertio-gravity waves, which propagate vertically upward from near the RCB. We showed in detail that the QBO-like oscillations in our models are driven by the interaction of these waves with the mean flow; in particular, absorption of waves at critical levels on the lower flanks of the stacked eastward and westward equatorial stratospheric jets causes the jets to migrate downward over time.
5. Some of our models produce zonal-jet profiles very similar to those on Jupiter and Saturn, including stable, long-lived equatorial superrotation in the troposphere, numerous high-latitude jets, and hints of polar cyclones that resemble Saturn's hexagon.

Our results support a picture wherein the convective forcing triggers a population of Rossby waves, the latitudinally preferential breaking of which leads to a coherent zonal jet structure with eastward eddy acceleration in the eastward jets and westward eddy acceleration in the westward jets. As proposed by Showman & Kaspi (2013), such jet accelerations cause an overturning circulation in the meridional plane. The vertical motion associated with this circulation transports entropy vertically and leads to horizontal temperature perturbations on isobars, even in the absense of any externally imposed irradiation gradients. In a model with clouds, the vertical motions associated with these overturning circulations would lead to patchy clouds, which will help to explain the light curve variability observed on a wide range of brown dwarfs.

Our models show that the atmosphere of brown dwarfs and giant planets can exhibit the emergence of oscillations having timescales orders of magnitude longer than any of the explicit forcing and damping timescales. The implication is that brown dwarfs are likely to be variable not only on short timescales (as has already been extensively observed) but on longer timescales of years or even decades as well, despite the fact that the radiative and convective timescales are likely short on these objects.

The existence of banded flow patterns in all our models—including those with very strong radiative damping—differs from the results reported by Zhang & Showman (2014), who used a one-layer shallow-water model and found that, when the forcing was weak and/or the damping was strong, the flow transitioned to an isotropic state dominated by turbulent eddies with no (statistically) preferred directionality. The differing behavior results from the fact that, in 3D models, radiative damping can remove horizontal temperature variations and therefore (via the thermal-wind equation) vertical wind shears, but it cannot damp the barotropic mode—that is, the pressure-independent component of the wind, which is not associated with any horizontal temperature gradients. Essentially, by assuming a quiescent interior underlying their one-layer atmosphere, Zhang & Showman (2014) assumed that there is no barotropic mode. In our 3D models, the barotropic mode can be damped by the friction imposed near the base of our model. In the present context, then, the setup of Zhang & Showman (2014) would best be represented by the limit of very strong drag at the base of the model.

Our model setup—with idealized convective forcing and radiative damping—represents a useful platform for further dynamical studies of the Jovian QQO, Saturnian SAO, and potentially even Earth's QBO. Inclusion of gravity-wave-drag parameterizations and further exploration of the large model parameter space may yield a more complete understanding of the conditions under which these oscillations occur, including the amplitude, wavenumber, and latitudinal profile of convective wave forcing that yield oscillations in agreement with observations. Moreover, it would be straightforward to add a simple seasonal cycle, relevant to Saturn and Earth, which would allow an investigation of how QBO-like oscillations interact with a seasonally varying stratospheric meridional circulation. This is relevant to understanding the tendency of the QBO to "lock onto" the seasonal cycle (e.g., Rajendran et al. 2016, 2018) and may be important for understanding why Saturn's SAO has a period close to half a Saturn year. Moreover, both the terrestrial QBO and Saturn's SAO have recently experienced disruptions (Dunkerton 2016; Newman et al. 2016; Fletcher et al. 2017), a phenomenon that could be explored in our model framework by introducing perturbations to the convective forcing or seasonal cycle to determine how they affect the QBO-like oscillation properties.

Our models lack any representation of cloud feedbacks, which are likely important for the atmospheric dynamics on many brown dwarfs (e.g., Tan & Showman 2018). The heating and cooling associated with time-variable patchy clouds could lead to significant horizontal temperature variations due purely to radiative effects, which in turn will be important in driving the atmospheric circulation, particularly on L dwarfs, which have relatively opaque clouds and extremely high heat fluxes due to their high temperatures. Including such cloud feedbacks in 3D models of this type is an important avenue for future research. Nevertheless, the current, idealized, cloud-free models provide a critical foundation for understanding more complex scenarios. Moreover, our cloud-free models are likely directly relevant to a wide range of brown dwarfs where cloud effects are relatively weak, such as the mid-to-late T dwarfs, which exhibit relatively cloud-free atmospheres, or cooler giant planets (including Y dwarfs as well as Jupiter and Saturn themselves) where the lower temperatures imply that the cloud radiative forcing is likely to be weaker.

A.P.S. thanks the NSF (grant AST1313444) and Peking University for support.

Appendix
Forcing

Here, we physically motivate plausible forcing amplitudes that may be relevant to brown dwarfs of specified heat flux and other parameters. We imagine material surfaces just above the RCB being perturbed up and down by buoyant, rising convective plumes overshooting into the stratified atmosphere (or of descending plumes dripping off the bottom of the RCB into the interior). To represent these effects, thermal forcing is added to the thermodynamic-energy equation in a forcing layer in the bottom scale height of the domain, with the aim of deflecting material surfaces up and down in a way analogous to convection. Here, we estimate the expected amplitudes this forcing should have.

The specific question we seek to answer is: how do we select appropriate values of $f_{\rm amp}$, if we want to represent convection from a brown dwarf of some given heat flux? We break this into three steps. First, let us calculate the typical overshoot distance of plumes, Δz, given some vertical velocity at the RCB, which we could estimate from mixing length theory. Second, let us estimate, in our forcing scheme, what characteristic horizontal variations of temperature would be needed in the bottom scale height of our model to generate material-surface displacements of this magnitude, and third, we will determine what values of $f_{\rm amp}$ are needed to generate those necessary horizontal temperature variations.

A.1. Overshoot Distance of Convective Plumes at RCB

We first calculate the overshoot distance, Δz, for a rising convective plume of velocity w that overshoots across the RCB, given a specified background potential temperature gradient immediately above the RCB of $\partial\theta/\partial z$. If at some time t the parcel has ascended to a height $\Delta z'$, then the instantaneous difference in potential temperature between the parcel and its surroundings will be $\Delta\theta = -(\partial\theta/\partial z)\Delta z'$ and the negative buoyancy acceleration will be $-g\,\Delta\theta/\theta$. Using parcel theory, we simply write the equation of motion for the parcel as

$$\frac{d^2\Delta z'}{dt^2} = \frac{\Delta\theta}{\theta}g = -\frac{g}{\theta}\frac{\partial\theta}{\partial z}\Delta z', \tag{12}$$

which has solution $\Delta z' = \Delta z \sin Nt$, where N is the Brunt–Väisälä frequency and Δz is the maximum amplitude of the displacement (i.e., the height above the RCB at which the parcel reaches its maximum altitude and begins descending). The time-varying parcel velocity is just the time derivative of this solution, $d\Delta z'/dt = N\Delta z \cos Nt$, which has a maximum velocity amplitude of $N\Delta z$. Because this is just our assumed convective velocity, we can write that, given some velocity w at the RCB, the overshoot distance is

$$\Delta z \sim \frac{w}{N}. \tag{13}$$

In Equation (13), it is not obvious a priori what value of N would be appropriate, given that it depends both on the stratification above the RCB, as well as the gravity and other parameters, all of which might vary widely on brown dwarfs. Therefore, it is convenient to rewrite expression (13) using a simple dimensionless parameter that characterizes the subadiabaticity of the thermal profile. Following Zhang & Showman (2014), we define a "subadiabaticity parameter" $\gamma = 1 + (c_p/g)\partial T/\partial z = 1 - \kappa^{-1}\partial \ln T/\partial \ln p$, where $\kappa = R/c_p$ is the ratio of the specific gas constant to the specific heat at constant pressure. Using this definition, the Brunt–Väisälä frequency can be expressed as $N^2 = \frac{g^2}{Tc_p}\gamma$, where $\gamma = 1$ for an isothermal atmosphere and $\gamma = 0$ for an adiabatic atmosphere. What is an appropriate value of γ? Although the atmospheres of brown dwarfs should be quite stratified aloft (approaching an isotherm at high altitude according to 1D models; e.g., Burrows et al. 2006), the stratification should be weak just above the RCB, with only minimal deviations from an adiabat. Zhang & Showman (2014) suggested $\gamma = 0.1$ as appropriate. The value will depend on how sharply the thermal gradient transitions from adiabatic to isothermal above the RCB, and on how this distance compares to the overshoot distance.

It is convenient to express the overshoot distance in fractions of a scale height, i.e., from Equation (13), $\Delta z/H \sim w/NH$, where H is scale height. Within factors of order unity, NH is the phase speed of fast horizontal gravity waves (those with long vertical wavelengths). It can be shown that

$$\begin{aligned} NH &= \sqrt{RT}\left[\kappa - \frac{\partial \ln T}{\partial \ln p}\right]^{1/2} \\ &= \sqrt{RT\kappa}\left[1 - \frac{1}{\kappa}\frac{\partial \ln T}{\partial \ln p}\right]^{1/2} \equiv \sqrt{\gamma RT\kappa}\,. \end{aligned} \tag{14}$$

Combining Equations (13) and (14), one obtains a final expression for overshoot distance,

$$\frac{\Delta z}{H} \sim \frac{w}{\sqrt{\gamma RT\kappa}}. \tag{15}$$

From the perspective of the above equations, w is an independently specified parameter, but we can constrain it using mixing length theory for convection, which implies

$$w \sim \left(\frac{\alpha F g l}{\rho c_p}\right)^{1/3}, \tag{16}$$

where α is thermal expansivity, F is transported heat flux, l is mixing length, and ρ is density. Assuming ideal gas ($\alpha = 1/T$ and $\rho = p/RT$) and that the mixing length is a scale height, this becomes

$$w \sim \left(\frac{FR^2T}{pc_p}\right)^{1/3}, \tag{17}$$

which, for brown dwarf parameters ($F \sim 10^4$–$10^5\,\mathrm{W\,m^{-2}}$, $R = 3700\,\mathrm{J\,kg^{-1}\,K^{-1}}$, $T \sim 10^3\,\mathrm{K}$, $p \sim 10^6\,\mathrm{Pa}$ for the RCB, and $c_p = 10^4\,\mathrm{J\,kg^{-1}\,K^{-1}}$) yields $w \sim 20$–$50\,\mathrm{m\,s^{-1}}$. For a planet with Jupiter's heat flux ($\sim 10\,\mathrm{W\,m^{-2}}$), we obtain $w \sim 1$–$2\,\mathrm{m\,s^{-1}}$.

Combining Equations (15) and (17), we obtain overshoot distances

$$\frac{\Delta z}{H} \sim \left(\frac{F}{Rp}\right)^{1/3}\left(\frac{c_p}{T}\right)^{1/6}\frac{1}{\gamma^{1/2}}. \tag{18}$$

We are now in a position to obtain numerical estimates of the overshoot distance from Equation (15) or (18). Adopting

$\gamma = 0.1$, $R = 3700\,\mathrm{J\,kg^{-1}\,K^{-1}}$, $T = 1500\,\mathrm{K}$, and $\kappa = 2/7 = 0.2857$ appropriate for a diatomic H_2 atmosphere, along with the same range of heat fluxes as used when estimating the velocities, we obtain $\Delta z/H \sim 0.05$–0.12. In other words, mixing length theory suggests an overshoot distance on the order of 10% of a scale height, varying weakly as the heat flux to the one-third power. For a planet with Jupiter's heat flux, the appropriate value is order $\Delta z/H \sim 0.01$.

A.2. Required Temperature Perturbations in the Forced Layer

Our goal is for the parameterization to vertically perturb material surfaces by amplitudes comparable to that given in Equation (18). We now address this question: if we accomplish these displacements by imposing horizontally varying heating in the bottom ∼scale height of the model domain (following Equation (1)), then what amplitude of horizontal temperature variations in this "parameterized forcing" layer are needed in order to generate these deflections?

This can straightforwardly be estimated from hydrostatic balance applied to some local region, i.e.,

$$\frac{\partial \Phi}{\partial \ln p} = -RT, \tag{19}$$

which implies that the increment in height δz over some range of log pressures is given by

$$\delta\Phi = g\delta z \approx -RT\delta \ln p, \tag{20}$$

where δ is a vertical difference across some finite slab, such that $\delta \ln p$ is the range of log-pressures across the forced layer, and δz is the height (thickness) of the forced layer. Now imagine heating or cooling causes a change in temperature of the gas inside the forcing layer, such that we start with an initial temperature T_i and end with a final temperature T_f. This will change the thickness of the forcing layer following $g\delta z_i \approx -RT_i\delta \ln p$ and $g\delta z_f \approx -RT_f\delta \ln p$, where δz_i and δz_f are the initial and final vertical thicknesses of the forcing layer. (The pressure range of the forced layer does not change, so we adopt the same $\delta \ln p$ for the two states.) The difference in the thickness of the initial and final forcing layer is

$$\delta z_f - \delta z_i \approx -\frac{R(T_f - T_i)}{g}\delta \ln p. \tag{21}$$

In the limit of zero horizontal divergence, the entire overlying column will move up or down by this amount—in other words, this is the amplitude of vertical deflections of material surfaces in the air above the forced layer.[12] Thus, we expect that the deflections of material surfaces caused by temperature perturbations $\Delta T_{\mathrm{force}}$ that are applied over a vertical thickness of one scale height ($\delta \ln p = 1$) are on the order of

$$\Delta z \sim \frac{R\Delta T_{\mathrm{force}}}{g}. \tag{22}$$

Using the definition of scale height, this equation is simply $\Delta z/H \sim \Delta T_{\mathrm{force}}/T$. Adopting our earlier expression for vertical deflections, we thus require fractional temperature differences in the forcing layer of

$$\frac{\Delta T_{\mathrm{force}}}{T} \sim \frac{w}{\sqrt{\gamma RT\kappa}}, \tag{23}$$

which, as estimated previously, should have values of ∼0.05–0.12 for a typical range of conditions encountered on brown dwarfs, and as low as 0.01 for a Jupiter-like planet. A typical brown dwarf temperature of 1500 K above the RCB—and rounding—implies that we need temperature perturbations in the forcing layer on the order of 50–200 K, or even lower for a planet with a heat flux comparable to Jupiter.

A.3. Required Forcing Amplitudes

We now wish to determine the characteristic forcing amplitudes f_{amp} that are needed to achieve the desired $\Delta T_{\mathrm{force}}$ calculated above. We expect that, because the two terms on the right-hand side of Equation (4) are uncorrelated, the forcing will statistically equilibrate its amplitude such that

$$|S_h| \approx |\hat{F}|, \tag{24}$$

where $|\hat{F}|$ is the characteristic amplitude of F, the random modifier of the forcing (see Equation (4)), and $|S_h|$ is the characteristic amplitude of the forcing S_h. In Equation (6), the normalized Legendre polynomials each have characteristic values on the order of unity, as do the cosines multiplying them. A standard result is that adding N one-dimensional sinusoids of equal wavenumber, amplitude = 1, but random phases leads to a characteristic summed amplitude $\sqrt{N}$. Analogously, we expect that adding up n_f modes of equal total wavenumber but random phases should lead to a characteristic amplitude of order $\sqrt{n_f}$, implying from Equation (6) that $|\hat{F}| \sim f_{\mathrm{amp}}\sqrt{n_f}$. Thus,

$$|S_h| \approx f_{\mathrm{amp}}\sqrt{n_f}. \tag{25}$$

This forcing will cause the characteristic horizontal temperature contrasts to increase with time in the forcing layer, although not necessarily linearly with time, because at any given location, the sign of S_h can change from positive to negative over characteristic timescales τ_{for}, implying a degree of cancellation in how the forcing integrates in time. This growth of $\Delta T_{\mathrm{force}}$ will be resisted by the radiative damping in the system, and potentially also by horizontal advection if the horizontal winds in the forcing layer become sufficiently strong, causing $\Delta T_{\mathrm{force}}$ to statistically equilibrate. In the case where radiative timescales are sufficiently short for the radiation to comprise the dominant damping process, we could write

$$\frac{\Delta T_{\mathrm{force}}}{\tau_{\mathrm{rad}}} \sim f_{\mathrm{amp}}\sqrt{n_f}, \tag{26}$$

implying that the equilibrated temperature variations in the forcing layer have amplitude $\Delta T_{\mathrm{force}} \sim \tau_{\mathrm{rad}} f_{\mathrm{amp}}\sqrt{n_f}$. The model

[12] In principle, there could be subtle interactions with the dynamics, in that there will be horizontal divergence in regions where the forcing layer expands vertically, as well as horizontal convergence in regions where the forcing layer contracts vertically, which might conceivably lessen the actual vertical deflections of material surfaces in the atmosphere overlying the forcing layer, as compared to the case where we essentially suppress dynamics and imagine zero horizontal divergence. Still, this limit of zero horizontal divergence should be roughly correct for the case—relevant to our simulations—where the horizontal forcing scale is comparable to or larger than the Rossby deformation radius, because the rotation will tend to supress the ability of the fluid to expand/contract horizontally.

analyzed in Section 3.4, for example, has $\tau_{\rm rad} = 10^6$ s, $f_{\rm amp} = 5 \times 10^{-6}$ K s^{-1}, and $n_f = 20$, and the above equation predicts $\Delta T_{\rm force} \approx 25$ K, similar to the actual horizontal temperature contrasts at the bottom of the forcing layer, which fluctuate between 15 and 25 K once the forcing reaches a statistical equilibrium.

As a final step, we can rewrite the balance as an expression for the desired forcing amplitude, which, when the balance (26) dominates, yields

$$f_{\rm amp} \sim \frac{\Delta T_{\rm force}}{\tau_{\rm rad}\sqrt{n_f}} \sim \frac{\Delta z}{H}\frac{T}{\tau_{\rm rad}\sqrt{n_f}}, \quad (27)$$

where $\Delta z/H$ could be specified from Equation (18), and in the latter expression, we have used the fact that $\Delta T_{\rm force}/T \sim \Delta z/H$. Plugging in $\Delta z/H \sim 0.1$, a value appropriate for typical brown dwarfs, $\tau_{\rm rad} \sim 10^6$ s, $T = 1500$ K, and $n_f = 20$ yields $f_{\rm amp} \sim 3 \times 10^{-5}$ K s^{-1}, similar to our highly forced models. Adopting $\Delta z/H \sim 0.01$, which is relevant to a low, Jupiter-like heat flux, instead yields $f_{\rm amp} \sim 3 \times 10^{-6}$ K s^{-1}, similar to our weaker-forced models, including the model exhibiting a QBO-like oscillation analyzed in Section 3.4. Therefore, the forcing amplitudes adopted in this paper are appropriate for brown dwarfs and giant planets.

However, we emphasize that these estimates linking $f_{\rm amp}$ to objects of a particular heat flux should be taken as only a very rough guide, because there are many uncertainties, not only in the convective velocities and vertical thermal profile near the RCB (which controls γ) but in the processes that cause the convection to self-organize, which will determine whether the overshoot distance Δz relevant on the convective scale is also relevant on the scale of large-scale convective organization, as we have implicitly assumed. Moreover, the framework of thermal perturbations that we have adopted is only one approach; in the future, it may also be interesting to investigate alternate forcing schemes, such as the introduction of momentum forcing near the RCB, which might parameterize the effect of convective Reynolds stresses acting at the base of the stratified atmosphere.

ORCID iDs

Xianyu Tan https://orcid.org/0000-0003-2278-6932

References

Adcroft, A., Campin, J.-M., Hill, C., & Marshall, J. 2004, MWRv, 132, 2845
Andrews, D. G., Holton, J. R., & Leovy, C. B. 1987, Middle Atmosphere Dynamics (New York: Academic)
Andrews, D. G., Mahlman, J. D., & Sinclair, R. W. 1983, JAtS, 40, 2768
Apai, D., Karalidi, T., Marley, M. S., et al. 2017, Sci, 357, 683
Apai, D., Radigan, J., Buenzli, E., et al. 2013, ApJ, 768, 121
Artigau, É. 2018, in Handbook of Exoplanets, ed. H. J. Deeg & J. A. Belmonte (Cham: Springer)
Artigau, É., Bouchard, S., Doyon, R., & Lafrenière, D. 2009, ApJ, 701, 1534
Baines, K. H., Momary, T. W., Fletcher, L. N., et al. 2009, P&SS, 57, 1671
Baldwin, M. P., Gray, L. J., Dunkerton, T. J., et al. 2001, RvGeo, 39, 179
Biller, B. 2017, AstRv, 13, 1
Buenzli, E., Saumon, D., Marley, M. S., et al. 2015, ApJ, 798, 127
Burrows, A., Sudarsky, D., & Hubeny, I. 2006, ApJ, 650, 1140
Busse, F. H. 2002, PhFl, 14, 1301
Christensen, U. R. 2002, JFM, 470, 115
Conrath, B. J., Gierasch, P. J., & Leroy, S. S. 1990, Icar, 83, 255
Cosentino, R. G., Morales-Juberías, R., Greathouse, T., et al. 2017, JGRE, 122, 2719
Crossfield, I. J. M., Biller, B., Schlieder, J. E., et al. 2014, Natur, 505, 654
Cushing, M. C., Hardegree-Ullman, K. K., Trucks, J. L., et al. 2016, ApJ, 823, 152
Del Genio, A. D., Achterberg, R. K., Baines, K. H., et al. 2009, in Saturn from Cassini-Huygens, ed. M. K. Dougherty, L. W. Esposito, & S. M. Krimigis (Berlin: Springer), 113
Dritschel, D. G., & McIntyre, M. E. 2008, JAtS, 65, 855
Duarte, L. D. V., Gastine, T., & Wicht, J. 2013, PEPI, 222, 22
Dunkerton, T. J. 2016, GeoRL, 43, 10547
Esplin, T. L., Luhman, K. L., Cushing, M. C., et al. 2016, ApJ, 832, 58
Fletcher, L. N., Greathouse, T. K., Orton, G. S., et al. 2016, Icar, 278, 128
Fletcher, L. N., Guerlet, S., Orton, G. S., et al. 2017, NatAs, 1, 765
Fouchet, T., Guerlet, S., Strobel, D. F., et al. 2008, Natur, 453, 200
Freytag, B., Allard, F., Ludwig, H.-G., Homeier, D., & Steffen, M. 2010, A&A, 513, A19
Friedson, A. J. 1999, Icar, 137, 34
Friedson, A. J., & Moses, J. I. 2012, Icar, 218, 861
Guerlet, S., Fouchet, T., Bézard, B., Flasar, F. M., & Simon-Miller, A. A. 2011, GeoRL, 38, 9201
Guerlet, S., Fouchet, T., Spiga, A., et al. 2018, JGRE, 123, 246
Guerlet, S., Spiga, A., Sylvestre, M., et al. 2014, Icar, 238, 110
Hayashi, Y. 1971, J. Met. Soc. Japan, 49, 125
Heimpel, M., Aurnou, J., & Wicht, J. 2005, Natur, 438, 193
Helling, C., & Casewell, S. 2014, A&ARv, 22, 1
Holton, J. R., & Hakim, G. J. 2013, An Introduction to Dynamic Meteorology (5th ed.; San Diego: Academic)
Holton, J. R., & Lindzen, R. S. 1972, JAtS, 29, 1076
Ingersoll, A. P., Dowling, T. E., Gierasch, P. J., et al. 2004, Dynamics of Jupiter's atmosphere (Jupiter. The Planet, Satellites and Magnetosphere) (Cambridge: Cambridge Univ. Press), 105
Karalidi, T., Apai, D., Marley, M. S., & Buenzli, E. 2016, ApJ, 825, 90
Kaspi, Y., Flierl, G. R., & Showman, A. P. 2009, Icar, 202, 525
Kuroda, T., Medvedev, A. S., & Hartogh, P. 2014, Icar, 242, 149
Leggett, S. K., Cushing, M. C., Hardegree-Ullman, K. K., et al. 2016, ApJ, 830, 141
Leovy, C. B., Friedson, A. J., & Orton, G. S. 1991, Natur, 354, 380
Li, C., Le, T., Zhang, X., & Yung, Y. L. 2018a, JQSRT, 217, 353
Li, L., Jiang, X., West, R. A., et al. 2018b, NatCo, 9, 3709
Li, X., & Read, P. L. 2000, P&SS, 48, 637
Lian, Y., & Showman, A. P. 2008, Icar, 194, 597
Lian, Y., & Showman, A. P. 2010, Icar, 207, 373
Lilly, D. K. 1969, PhFl, 12, II240
Lindzen, R. S., & Holton, J. R. 1968, JAtS, 25, 1095
Liu, B., & Showman, A. P. 2013, ApJ, 770, 42
Liu, J., Goldreich, P. M., & Stevenson, D. J. 2008, Icar, 196, 653
Liu, J., & Schneider, T. 2010, JAtS, 67, 3652
Liu, J., & Schneider, T. 2011, JAtS, 68, 2742
Marley, M. S., & Robinson, T. D. 2015, ARA&A, 53, 279
Metchev, S. A., Heinze, A., Apai, D., et al. 2015, ApJ, 799, 154
Miles-Páez, P. A., Pallé, E., & Zapatero Osorio, M. R. 2017, MNRAS, 472, 2297
Morales-Juberías, R., Sayanagi, K. M., Simon, A. A., Fletcher, L. N., & Cosentino, R. G. 2015, ApJL, 806, L18
Morley, C. V., Skemer, A. J., Allers, K. N., et al. 2018, ApJ, 858, 97
Newman, P. A., Coy, L., Pawson, S., & Lait, L. R. 2016, GeoRL, 43, 8791
Nozawa, T., & Yoden, S. 1997, PhFl, 9, 2081
Orton, G. S., Friedson, A. J., Caldwell, J., et al. 1991, Sci, 252, 537
Orton, G. S., Yanamandra-Fisher, P. A., Fisher, B. M., et al. 2008, Natur, 453, 196
Plumb, R. A. 1977, JAtS, 34, 1847
Plumb, R. A. 1984, in Dynamics of the Middle Atmosphere, ed. J. R Holton & T. Matsuno (Tokyo: Terrapub), 217
Radigan, J., Jayawardhana, R., Lafrenière, D., et al. 2012, ApJ, 750, 105
Rajendran, K., Moroz, I. M., Osprey, S. M., & Read, P. L. 2018, JAtS, 75, 2281
Rajendran, K., Moroz, I. M., Read, P. L., & Osprey, S. M. 2016, QJRMS, 142, 1111
Randel, W. J., & Held, I. M. 1991, JAtS, 48, 688
Read, P. L., Conrath, B. J., Fletcher, L. N., et al. 2009, P&SS, 57, 1682
Reiners, A., & Basri, G. 2008, ApJ, 684, 1390
Robinson, T. D., & Marley, M. S. 2014, ApJ, 785, 158
Sánchez-Lavega, A., Sromovsky, L., Showman, A., et al. 2019, in Zonal Jets: Phenomenology, Genesis, and Physics, ed. B. Galperin & P. L. Read (Cambridge: Cambridge Univ. Press)
Schneider, T., & Liu, J. 2009, JAtS, 66, 579
Scott, R. K., & Dritschel, D. G. 2012, JFM, 711, 576
Scott, R. K., & Polvani, L. 2007, JAtS, 64, 3158

Showman, A. P. 2007, JAtS, 64, 3132
Showman, A. P., Cho, J. Y.-K., & Menou, K. 2010, in Exoplanets, ed. S. Seager (Tucson, AZ: Univ. Arizona Press), 471
Showman, A. P., & Guillot, T. 2002, A&A, 385, 166
Showman, A. P., Ingersoll, A. P., Achterberg, R., & Kaspi, Y. 2019, in Saturn in the 21st Century, ed. K. H. Baines & M. Flasar (Cambridge: Cambridge Univ. Press), 295
Showman, A. P., & Kaspi, Y. 2013, ApJ, 776, 85
Showman, A. P., Kaspi, Y., & Flierl, G. R. 2011, Icar, 211, 1258
Showman, A. P., Wordsworth, R. D., Merlis, T. M., & Kaspi, Y. 2013, in Comparative Climatology of Terrestrial Planets, ed. S. J. Mackwell et al. (Tucson, AZ: Univ. Arizona Press), 277
Simon-Miller, A. A., Conrath, B. J., Gierasch, P. J., et al. 2006, Icar, 180, 98
Skemer, A. J., Morley, C. V., Allers, K. N., et al. 2016, ApJL, 826, L17
Sukoriansky, S., Dikovskaya, N., & Galperin, B. 2007, JAtS, 64, 3312
Takahashi, M. 1996, GeoRL, 23, 661
Takahashi, M. 1999, GeoRL, 26, 1307
Tan, X., & Showman, A. P. 2017, ApJ, 835, 186
Tan, X., & Showman, A. P. 2018, ApJ, 874, 111
Vallis, G. K. 2006, Atmospheric and Oceanic Fluid Dynamics: Fundamentals and Large-Scale Circulation (Cambridge: Cambridge Univ. Press)
Vasavada, A. R., & Showman, A. P. 2005, RPPh, 68, 1935
Wheeler, M., & Kiladis, G. N. 1999, JAtS, 56, 374
Williams, G. P. 1978, JAtS, 35, 1399
Williams, G. P. 1979, JAtS, 36, 932
Williams, G. P. 2003, JAtS, 60, 1270
Wilson, P. A., Rajan, A., & Patience, J. 2014, A&A, 566, A111
Yang, H., Apai, D., Marley, M. S., et al. 2016, ApJ, 826, 8
Young, R. M. B., Read, P. L., & Wang, Y. 2019, Icar, 326, 225
Zhang, X., & Showman, A. P. 2014, ApJL, 788, L6